Double-spin asymmetry of electrons from heavy-flavor decays in $p + p$ collisions at $\sqrt{s} = 200$ GeV

A. Adare,[11] S. Afanasiev,[26] C. Aidala,[34] N. N. Ajitanand,[56] Y. Akiba,[50,51] R. Akimoto,[10] H. Al-Ta'ani,[44] J. Alexander,[56] K. R. Andrews,[1] A. Angerami,[12] K. Aoki,[50] N. Apadula,[57] E. Appelt,[61] Y. Aramaki,[10,50] R. Armendariz,[6] E. C. Aschenauer,[5] T. C. Awes,[46] B. Azmoun,[5] V. Babintsev,[21] M. Bai,[4] B. Bannier,[57] K. N. Barish,[6] B. Bassalleck,[43] A. T. Basye,[1] S. Bathe,[51] V. Baublis,[49] C. Baumann,[39] A. Bazilevsky,[5] R. Belmont,[61] J. Ben-Benjamin,[40] R. Bennett,[57] A. Berdnikov,[53] Y. Berdnikov,[53] D. S. Blau,[30] J. S. Bok,[64] K. Boyle,[51] M. L. Brooks,[34] D. Broxmeyer,[40] H. Buesching,[5] V. Bumazhnov,[21] G. Bunce,[5,51] S. Butsyk,[34] S. Campbell,[57] P. Castera,[57] C.-H. Chen,[57] C. Y. Chi,[12] M. Chiu,[5] I. J. Choi,[22,64] J. B. Choi,[8] R. K. Choudhury,[3] P. Christiansen,[36] T. Chujo,[60] O. Chvala,[6] V. Cianciolo,[46] Z. Citron,[57] B. A. Cole,[12] Z. Conesa del Valle,[32] M. Connors,[57] M. Csanád,[15] T. Csörgő,[63] S. Dairaku,[31,50] A. Datta,[38] G. David,[5] M. K. Dayananda,[18] A. Denisov,[21] A. Deshpande,[51,57] E. J. Desmond,[5] K. V. Dharmawardane,[44] O. Dietzsch,[54] A. Dion,[25] M. Donadelli,[54] O. Drapier,[32] A. Drees,[57] K. A. Drees,[4] J. M. Durham,[57] A. Durum,[21] L. D'Orazio,[37] Y. V. Efremenko,[46] T. Engelmore,[12] A. Enokizono,[46] H. En'yo,[50,51] S. Esumi,[60] B. Fadem,[40] D. E. Fields,[43] M. Finger,[7] M. Finger, Jr.,[7] F. Fleuret,[32] S. L. Fokin,[30] J. E. Frantz,[45] A. Franz,[5] A. D. Frawley,[17] Y. Fukao,[50] T. Fusayasu,[42] I. Garishvili,[58] A. Glenn,[33] X. Gong,[56] M. Gonin,[32] Y. Goto,[50,51] R. Granier de Cassagnac,[32] N. Grau,[12] S. V. Greene,[61] M. Grosse Perdekamp,[22] T. Gunji,[10] L. Guo,[34] H.-Å. Gustafsson,[36,*] J. S. Haggerty,[5] K. I. Hahn,[16] H. Hamagaki,[10] J. Hamblen,[58] R. Han,[48] J. Hanks,[12] C. Harper,[40] K. Hashimoto,[50,52] E. Haslum,[36] R. Hayano,[10] X. He,[18] T. K. Hemmick,[57] T. Hester,[6] J. C. Hill,[25] R. S. Hollis,[6] W. Holzmann,[12] K. Homma,[20] B. Hong,[29] T. Horaguchi,[60] Y. Hori,[10] D. Hornback,[46] S. Huang,[61] T. Ichihara,[50,51] R. Ichimiya,[50] H. Iinuma,[28] Y. Ikeda,[50,52,60] K. Imai,[31,50] M. Inaba,[60] A. Iordanova,[6] D. Isenhower,[1] M. Ishihara,[50] M. Issah,[61] A. Isupov,[26] D. Ivanischev,[49] Y. Iwanaga,[20] B. V. Jacak,[57,†] J. Jia,[5,56] X. Jiang,[34] D. John,[58] B. M. Johnson,[5] T. Jones,[1] K. S. Joo,[41] D. Jouan,[47] J. Kamin,[57] S. Kaneti,[57] B. H. Kang,[19] J. H. Kang,[64] J. S. Kang,[19] J. Kapustinsky,[34] K. Karatsu,[31,50] M. Kasai,[50,52] D. Kawall,[38,51] A. V. Kazantsev,[30] T. Kempel,[25] A. Khanzadeev,[49] K. M. Kijima,[20] B. I. Kim,[29] D. J. Kim,[27] E.-J. Kim,[8] Y.-J. Kim,[22] Y. K. Kim,[19] E. Kinney,[11] Á. Kiss,[15] E. Kistenev,[5] D. Kleinjan,[6] P. Kline,[57] L. Kochenda,[49] B. Komkov,[49] M. Konno,[60] J. Koster,[22] D. Kotov,[49] A. Král,[13] G. J. Kunde,[34] K. Kurita,[50,52] M. Kurosawa,[50] Y. Kwon,[64] G. S. Kyle,[44] R. Lacey,[56] Y. S. Lai,[12] J. G. Lajoie,[25] A. Lebedev,[25] D. M. Lee,[34] J. Lee,[16] K. B. Lee,[29] K. S. Lee,[29] S. H. Lee,[57] S. R. Lee,[8] M. J. Leitch,[34] M. A. L. Leite,[54] X. Li,[9] S. H. Lim,[64] L. A. Linden Levy,[11] A. Litvinenko,[26] H. Liu,[34] M. X. Liu,[34] B. Love,[61] D. Lynch,[5] C. F. Maguire,[61] Y. I. Makdisi,[4] A. Malakhov,[26] A. Manion,[57] V. I. Manko,[30] E. Mannel,[12] Y. Mao,[48,50] H. Masui,[60] M. McCumber,[57] P. L. McGaughey,[34] D. McGlinchey,[17] C. McKinney,[22] N. Means,[57] M. Mendoza,[6] B. Meredith,[22] Y. Miake,[60] T. Mibe,[28] A. C. Mignerey,[37] K. Miki,[50,60] A. Milov,[62] J. T. Mitchell,[5] Y. Miyachi,[50,59] A. K. Mohanty,[3] H. J. Moon,[41] Y. Morino,[10] A. Morreale,[6] D. P. Morrison,[5] S. Motschwiller,[40] T. V. Moukhanova,[30] T. Murakami,[31] J. Murata,[50,52] S. Nagamiya,[28] J. L. Nagle,[11] M. Naglis,[62] M. I. Nagy,[63] I. Nakagawa,[50,51] Y. Nakamiya,[20] K. R. Nakamura,[31,50] T. Nakamura,[50] K. Nakano,[50] J. Newby,[33] M. Nguyen,[57] M. Nihashi,[20] R. Nouicer,[5] A. S. Nyanin,[30] C. Oakley,[18] E. O'Brien,[5] C. A. Ogilvie,[25] M. Oka,[60] K. Okada,[51] A. Oskarsson,[36] M. Ouchida,[20,50] K. Ozawa,[10] R. Pak,[5] V. Pantuev,[23,57] V. Papavassiliou,[44] B. H. Park,[19] I. H. Park,[16] S. K. Park,[29] S. F. Pate,[44] H. Pei,[25] J.-C. Peng,[22] H. Pereira,[14] V. Peresedov,[26] D. Yu. Peressounko,[30] R. Petti,[57] C. Pinkenburg,[5] R. P. Pisani,[5] M. Proissl,[57] M. L. Purschke,[5] H. Qu,[18] J. Rak,[27] I. Ravinovich,[62] K. F. Read,[46,58] K. Reygers,[39] V. Riabov,[49] Y. Riabov,[49] E. Richardson,[37] D. Roach,[61] G. Roche,[35] S. D. Rolnick,[6] M. Rosati,[25] S. S. E. Rosendahl,[36] P. Rukoyatkin,[26] B. Sahlmueller,[39,57] N. Saito,[28] T. Sakaguchi,[5] V. Samsonov,[49] S. Sano,[10] M. Sarsour,[18] T. Sato,[60] M. Savastio,[57] S. Sawada,[28] K. Sedgwick,[6] R. Seidl,[51] R. Seto,[6] D. Sharma,[62] I. Shein,[21] T.-A. Shibata,[50,59] K. Shigaki,[20] H. H. Shim,[29] M. Shimomura,[60] K. Shoji,[31,50] P. Shukla,[3] A. Sickles,[5] C. L. Silva,[25] D. Silvermyr,[46] C. Silvestre,[14] K. S. Sim,[29] B. K. Singh,[2] C. P. Singh,[2] V. Singh,[2] M. Slunečka,[7] T. Sodre,[40] R. A. Soltz,[33] W. E. Sondheim,[34] S. P. Sorensen,[58] I. V. Sourikova,[5] P. W. Stankus,[46] E. Stenlund,[36] S. P. Stoll,[5] T. Sugitate,[20] A. Sukhanov,[5] J. Sun,[57] J. Sziklai,[63] E. M. Takagui,[54] A. Takahara,[10] A. Taketani,[50,51] R. Tanabe,[60] Y. Tanaka,[42] S. Taneja,[57] K. Tanida,[55,31,50] M. J. Tannenbaum,[5] S. Tarafdar,[2] A. Taranenko,[56] E. Tennant,[44] H. Themann,[57] D. Thomas,[1] M. Togawa,[51] L. Tomášek,[24] M. Tomášek,[24] H. Torii,[20] R. S. Towell,[1] I. Tserruya,[62] Y. Tsuchimoto,[20] K. Utsunomiya,[10] C. Vale,[5] H. W. van Hecke,[34] E. Vazquez-Zambrano,[12] A. Veicht,[12] J. Velkovska,[61] R. Vértesi,[63] M. Virius,[13] A. Vossen,[22] V. Vrba,[24] E. Vznuzdaev,[49] X. R. Wang,[44] D. Watanabe,[20] K. Watanabe,[60] Y. Watanabe,[50,51] Y. S. Watanabe,[10] F. Wei,[25] R. Wei,[56] J. Wessels,[39] S. N. White,[5] D. Winter,[12] C. L. Woody,[5] R. M. Wright,[1] M. Wysocki,[11] Y. L. Yamaguchi,[10] R. Yang,[22] A. Yanovich,[21] J. Ying,[18] S. Yokkaichi,[50,51] J. S. Yoo,[16] Z. You,[34,48] G. R. Young,[46] I. Younus,[43] I. E. Yushmanov,[30] W. A. Zajc,[12] A. Zelenski,[4] S. Zhou,[9] and L. Zolin[26]

(PHENIX Collaboration)

[1]*Abilene Christian University, Abilene, Texas 79699, USA*
[2]*Department of Physics, Banaras Hindu University, Varanasi 221005, India*
[3]*Bhabha Atomic Research Centre, Bombay 400 085, India*
[4]*Collider-Accelerator Department, Brookhaven National Laboratory, Upton, New York 11973-5000, USA*
[5]*Physics Department, Brookhaven National Laboratory, Upton, New York 11973-5000, USA*
[6]*University of California - Riverside, Riverside, California 92521, USA*
[7]*Charles University, Ovocný trh 5, Praha 1, 116 36, Prague, Czech Republic*
[8]*Chonbuk National University, Jeonju, 561-756, Korea*
[9]*Science and Technology on Nuclear Data Laboratory, China Institute of Atomic Energy, Beijing 102413, People's Republic of China*
[10]*Center for Nuclear Study, Graduate School of Science, University of Tokyo, 7-3-1 Hongo, Bunkyo, Tokyo 113-0033, Japan*
[11]*University of Colorado, Boulder, Colorado 80309, USA*
[12]*Columbia University, New York, New York 10027 and Nevis Laboratories, Irvington, New York 10533, USA*
[13]*Czech Technical University, Zikova 4, 166 36 Prague 6, Czech Republic*
[14]*Dapnia, CEA Saclay, F-91191, Gif-sur-Yvette, France*
[15]*ELTE, Eötvös Loránd University, H - 1117 Budapest, Pázmány P. s. 1/A, Hungary*
[16]*Ewha Womans University, Seoul 120-750, Korea*
[17]*Florida State University, Tallahassee, Florida 32306, USA*
[18]*Georgia State University, Atlanta, Georgia 30303, USA*
[19]*Hanyang University, Seoul 133-792, Korea*
[20]*Hiroshima University, Kagamiyama, Higashi-Hiroshima 739-8526, Japan*
[21]*IHEP Protvino, State Research Center of Russian Federation, Institute for High Energy Physics, Protvino, 142281, Russia*
[22]*University of Illinois at Urbana-Champaign, Urbana, Illinois 61801, USA*
[23]*Institute for Nuclear Research of the Russian Academy of Sciences, prospekt 60-letiya Oktyabrya 7a, Moscow 117312, Russia*
[24]*Institute of Physics, Academy of Sciences of the Czech Republic, Na Slovance 2, 182 21 Prague 8, Czech Republic*
[25]*Iowa State University, Ames, Iowa 50011, USA*
[26]*Joint Institute for Nuclear Research, 141980 Dubna, Moscow Region, Russia*
[27]*Helsinki Institute of Physics and University of Jyväskylä, P.O. Box 35, FI-40014 Jyväskylä, Finland*
[28]*KEK, High Energy Accelerator Research Organization, Tsukuba, Ibaraki 305-0801, Japan*
[29]*Korea University, Seoul, 136-701, Korea*
[30]*Russian Research Center "Kurchatov Institute", Moscow, 123098 Russia*
[31]*Kyoto University, Kyoto 606-8502, Japan*
[32]*Laboratoire Leprince-Ringuet, Ecole Polytechnique, CNRS-IN2P3, Route de Saclay, F-91128, Palaiseau, France*
[33]*Lawrence Livermore National Laboratory, Livermore, California 94550, USA*
[34]*Los Alamos National Laboratory, Los Alamos, New Mexico 87545, USA*
[35]*LPC, Université Blaise Pascal, CNRS-IN2P3, Clermont-Fd, 63177 Aubiere Cedex, France*
[36]*Department of Physics, Lund University, P.O. Box 118, SE-221 00 Lund, Sweden*
[37]*University of Maryland, College Park, Maryland 20742, USA*
[38]*Department of Physics, University of Massachusetts, Amherst, Massachusetts 01003-9337, USA*
[39]*Institut fur Kernphysik, University of Muenster, D-48149 Muenster, Germany*
[40]*Muhlenberg College, Allentown, Pennsylvania 18104-5586, USA*
[41]*Myongji University, Yongin, Kyonggido 449-728, Korea*
[42]*Nagasaki Institute of Applied Science, Nagasaki-shi, Nagasaki 851-0193, Japan*
[43]*University of New Mexico, Albuquerque, New Mexico 87131, USA*
[44]*New Mexico State University, Las Cruces, New Mexico 88003, USA*
[45]*Department of Physics and Astronomy, Ohio University, Athens, Ohio 45701, USA*
[46]*Oak Ridge National Laboratory, Oak Ridge, Tennessee 37831, USA*
[47]*IPN-Orsay, Universite Paris Sud, CNRS-IN2P3, BP1, F-91406, Orsay, France*
[48]*Peking University, Beijing 100871, People's Republic of China*
[49]*PNPI, Petersburg Nuclear Physics Institute, Gatchina, Leningrad region, 188300, Russia*
[50]*RIKEN Nishina Center for Accelerator-Based Science, Wako, Saitama 351-0198, Japan*
[51]*RIKEN BNL Research Center, Brookhaven National Laboratory, Upton, New York 11973-5000, USA*
[52]*Physics Department, Rikkyo University, 3-34-1 Nishi-Ikebukuro, Toshima, Tokyo 171-8501, Japan*
[53]*Saint Petersburg State Polytechnic University, St. Petersburg, 195251, Russia*
[54]*Universidade de São Paulo, Instituto de Física, Caixa Postal 66318, São Paulo CEP05315-970, Brazil*
[55]*Seoul National University, Seoul, Korea*
[56]*Chemistry Department, Stony Brook University, SUNY, Stony Brook, New York 11794-3400, USA*
[57]*Department of Physics and Astronomy, Stony Brook University, SUNY, Stony Brook, New York 11794-3400, USA*

[58]University of Tennessee, Knoxville, Tennessee 37996, USA
[59]Department of Physics, Tokyo Institute of Technology, Oh-okayama, Meguro, Tokyo 152-8551, Japan
[60]Institute of Physics, University of Tsukuba, Tsukuba, Ibaraki 305, Japan
[61]Vanderbilt University, Nashville, Tennessee 37235, USA
[62]Weizmann Institute, Rehovot 76100, Israel
[63]Institute for Particle and Nuclear Physics, Wigner Research Centre for Physics, Hungarian Academy of Sciences (Wigner RCP, RMKI) H-1525 Budapest 114, P.O. Box 49, Budapest, Hungary
[64]Yonsei University, IPAP, Seoul 120-749, Korea

(Received 17 September 2012; published 29 January 2013)

We report on the first measurement of the double-spin asymmetry, A_{LL}, of electrons from the decays of hadrons containing heavy flavor in longitudinally polarized $p + p$ collisions at $\sqrt{s} = 200$ GeV for $p_T = 0.5$ to 3.0 GeV/c. The asymmetry was measured at midrapidity ($|\eta| < 0.35$) with the PHENIX detector at the Relativistic Heavy Ion Collider. The measured asymmetries are consistent with zero within the statistical errors. We obtained a constraint for the polarized gluon distribution in the proton of $|\Delta g/g(\log_{10}x = -1.6^{+0.5}_{-0.4}, \mu = m_T^c)|^2 < 0.030$ (1σ) based on a leading-order perturbative quantum chromodynamics model, using the measured asymmetry.

DOI: 10.1103/PhysRevD.87.012011 PACS numbers: 13.85.Ni, 13.88.+e, 14.20.Dh, 25.75.Dw

I. INTRODUCTION

The measurement of the first moment of the proton's spin-dependent structure function g_1^p by the European Muon Collaboration [1,2] revealed a discrepancy from the Ellis-Jaffe sum rule [3,4] and also the fact that the SU(3) flavor-singlet axial charge $g_A^{(0)}$ was smaller than expected from the static and relativistic quark models [5]. After these discoveries, experimental efforts [6–8] focused on a detailed understanding of the spin structure of the proton. The proton spin $s_z/\hbar = 1/2$ can be decomposed as $\frac{1}{2} = \frac{1}{2}\Delta\Sigma + \Delta G + L_z$ from conservation of angular momentum. The measurements precisely determined the total spin carried by quarks and antiquarks, $\Delta\Sigma$, which is only about 30% of the proton spin. The remaining proton spin can be attributed to the other components, the gluon spin contribution (ΔG) and/or orbital angular momentum contributions (L_z). The total gluon polarization is given by

$$\Delta G(\mu) \equiv \int_0^1 dx \Delta g(x, \mu), \tag{1}$$

where x and μ represent Bjorken x and factorization scale, respectively. The challenge for the $\Delta G(\mu)$ determination is to precisely map the gluon polarization density $\Delta g(x, \mu)$ over a wide range of x.

The Relativistic Heavy Ion Collider (RHIC), which can accelerate polarized proton beams up to 255 GeV, is a unique and powerful facility to study the gluon polarization. One of the main goals of the RHIC physics program is to determine the gluon polarization through measurements of longitudinal double-spin asymmetries,

$$A_{LL} \equiv \frac{\sigma^{++} - \sigma^{+-}}{\sigma^{++} + \sigma^{+-}}, \tag{2}$$

where σ^{++} and σ^{+-} denote the cross sections of a specific process in the polarized $p + p$ collisions with same and opposite helicities. Using A_{LL}, the polarized cross sections, σ^{++} and σ^{+-}, can be represented as

$$\sigma^{+\pm} = \sigma_0(1 \pm A_{LL}), \tag{3}$$

where σ_0 is the unpolarized cross section of the process. A_{LL} has been measured previously in several channels by PHENIX and STAR, including inclusive π^0 [9–12], η [13], and jet [14–16] production.

Using the measured asymmetries, as well as the world data on polarized inclusive and semi-inclusive deep inelastic scattering [6–8,17,18], a global analysis based on perturbative quantum chromodynamics (pQCD) calculation was performed at next-to-leading order (NLO) in the strong coupling constant α_S [19]. The resulting $\Delta g(x, \mu)$ from the best fit is too small to explain the proton spin in the Bjorken x range of $0.05 < x < 0.2$ ($-1.3 < \log_{10}x < -0.7$) without considering L_z, though a substantial gluon polarization is not ruled out yet due to the uncertainties. Also, due to the limited Bjorken x coverage, there is a sizable uncertainty in Eq. (1) from the unexplored small x region.

The polarized cross section of heavy-flavor production on the partonic level is well studied with leading-order (LO) and NLO pQCD calculations [20–22]. The heavy quarks are produced dominantly by the gluon-gluon interaction at the partonic level [23]. Therefore, this channel has good sensitivity to the polarized gluon density. In addition, the large mass of the heavy quark ensures that pQCD techniques are applicable for calculations of the cross section. Therefore, the measurement of heavy-flavor production in polarized proton collisions is a useful tool to study gluon polarization.

In $p + p$ collisions at $\sqrt{s} = 200$ GeV, the heavy-flavor production below $p_T \sim 5$ GeV/c is dominated by charm quarks. The Bjorken x region covered by this process at

*Deceased.
†PHENIX Spokesperson.
jacak@skipper.physics.sunysb.edu

midrapidity is centered around $2m_c/\sqrt{s} \sim 1.4 \times 10^{-2}$ where m_c represents the charm quark mass. Hence, measurement of the spin-dependent heavy-flavor production is sensitive to the unexplored x region and complements other data on the total gluon polarization $\Delta G(\mu)$.

At PHENIX, hadrons containing heavy flavors are measured through their semileptonic decays to electrons and positrons, which are called "heavy flavor electrons" (HFe) [24,25]. Therefore, the double-spin asymmetry of the heavy flavor electrons is an important measurement for the gluon polarization study. In this paper, we report the first measurement of this asymmetry and a resulting constraint on the gluon polarization with a LO pQCD calculation. For the sake of simplicity, we use the word "electron" to include both electron and positron throughout this paper and distinguish by charge where necessary.

II. EXPERIMENTAL SETUP

This measurement is performed with the PHENIX detector positioned at one of the collision points at RHIC. The RHIC accelerator comprises a "blue ring" circulating clockwise and a "yellow ring" circulating counterclockwise. For this experiment, polarized bunches are stored and accelerated up to 100 GeV in each ring and collide with longitudinal polarizations of ~57% along the beams at the collision point with a collision energy of $\sqrt{s} = 200$ GeV. The bunch polarizations are changed to parallel (beam helicity +) or antiparallel (beam helicity −) along the beams alternately in the collisions to realize all $4 (= 2 \times 2)$ combinations of the crossing beam helicities. Each time the accelerator is filled, the pattern of beam helicities in the bunches is changed in order to confirm the absence of a pattern dependence of the measured spin asymmetry.

A detailed description of the complete PHENIX detector system can be found elsewhere [26–32]. The main detectors that are used in this analysis are beam-beam counters (BBC), zero degree calorimeters (ZDC), and two central arm spectrometers. The BBC provides the collision vertex information and the minimum bias (MB) trigger. The luminosity is determined by the number of MB triggers. Electrons are measured with the two central spectrometer arms which each cover a pseudorapidity range of $|\eta| < 0.35$ and azimuthal angle $\Delta\phi = \pi/2$.

Figure 1 shows the beam view of the 2009 PHENIX central arms configuration, which comprises the central magnet (CM), drift chamber (DC), and pad chamber (PC) (for charged particle tracking), the ring-imaging Čerenkov detector (RICH) and hadron blind detector (HBD) [33,34] (for electron identification) and the electromagnetic calorimeter (EMCal) (for energy measurement). The paper describes the first electron measurement made with the HBD, which was installed in 2009. Below, we summarize the features of the detectors and the CM.

The BBCs are two identical counters positioned at ±1.44 m from the nominal interaction point along the beam direction and cover pseudorapidity of $3.1 < |\eta| < 3.9$. They measure the collision vertex along the beam axis by measuring the time difference between the two counters and also provide the MB trigger defined by at least one hit on each side of the vertex. The position resolution for the vertex along the beam axis is ~2.0 cm in $p + p$ collision.

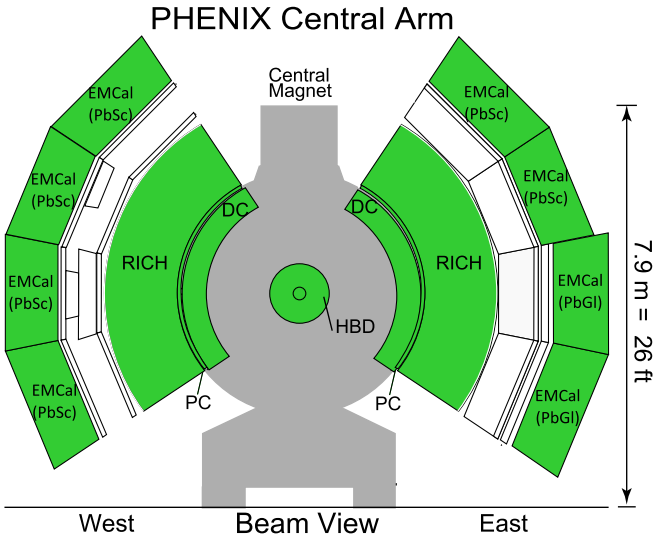

FIG. 1 (color online). Beam view (at $z = 0$) of the PHENIX central arm detectors in 2009. See text for details.

The ZDCs, which are located at ±18.0 m away from the nominal interaction point along the beam direction, detect neutral particles near the beam axis ($\theta < 2.5$ mrad). Along with the BBCs, the trigger counts recorded by the ZDCs are used to determine the relative luminosity between crossings with different beam helicity combinations. The ZDCs also serve for monitoring the orientation of the beam polarization in the PHENIX interaction region.

The transverse momentum of a charged particle track is determined by its curvature in the magnetic field provided by the PHENIX CM system [27]. The CM is energized by two pairs of concentric coils and provides an axial magnetic field parallel to the beam direction. The two coils of the CM were operated in the canceling ("+−") configuration, which is essential for the background rejection in the heavy flavor electron measurement accomplished using the HBD. The magnetic field is minimal in the radial region $0 < R < 50$ cm and has a peak value of ~0.35 T at $R \sim 100$ cm. The total field integral is $|\int B \times dl| = 0.43$ Tm.

The DC and PC in the central arms are used to track charged particles in the azimuthal direction to determine the transverse momentum (p_T) of each particle. From the polar angle measured by the PC and the BBC vertex information along the beam axis, the total momentum p is determined. The DC is positioned between 202 cm and 246 cm in radial distance from the collision point for both the west and east arms, and the PC is located at 247–252 cm.

The RICH is a threshold Čerenkov counter and is used to identify electrons in PHENIX. It is located in the radial

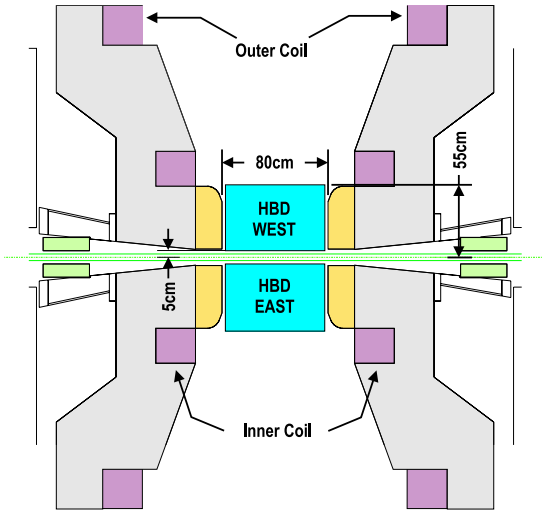

(a) HBD from top view.

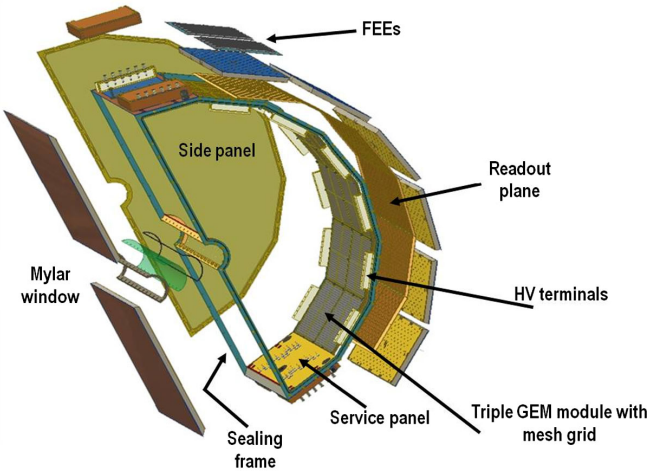

(b) Exploded view of one HBD arm.

FIG. 2 (color online). (a) Top view of the HBD showing the location of the HBD in the central magnet. (b) Exploded view of one HBD arm, which is half of the total HBD. CF_4 gas is filled in the volume as the Čerenkov light radiator.

region of 2.5–4.1 m. The RICH has a Čerenkov threshold of $\gamma = 35$, which corresponds to $p = 20$ MeV/c for electrons and $p = 4.9$ GeV/c for charged pions.

The EMCal comprises four rectangular sectors in each arm. The six sectors based on lead-scintillator calorimetry and the two (lowest sectors on the east arm) based on lead-glass calorimetry are positioned at radial distances from the collision point of ~5.1 m and ~5.4 m, respectively.

A challenging issue for the heavy flavor electron measurement is to reject the dominant background of electron pairs from γ conversions and Dalitz decays of π^0 and η mesons, which are mediated by virtual photons. These electrons are called "photonic electrons," while all the other electrons are called "nonphotonic electrons." Most nonphotonic electrons are from heavy-flavor decays. However, electrons from K_{e3} decays ($K \rightarrow e\nu\pi$) and the dielectron decays of light vector mesons are also nonphotonic [24]. The HBD is used to reduce the photonic electron pair background utilizing a distinctive feature of the e^+e^- pairs, namely, their small opening angles.

The HBD is a position-sensitive Čerenkov detector operated with pure CF_4 gas as a radiator. It covers the pseudorapidity range $|\eta| < 0.45$ and $2 \times 3\pi/4$ in azimuth. The coverage is larger than the acceptance of the other detectors in the central arm in order to detect photonic electron pairs with only one track reconstructed in the central arm and the other outside of the central arm acceptance. Figure 2 shows a top view and exploded view of the HBD. The HBD has a 50 cm long radiator directly coupled in a windowless configuration to a readout element consisting of a triple gas electron multiplier (GEM) stack, with a CsI photocathode evaporated on the top surface of the GEM facing the collision point and a pad readout at the exterior of the stack. The readout element in each HBD arm is divided into five sectors. The expected number of photoelectrons for an electron track is about 20, which is consistent with the measured number. Since the HBD is placed close to the collision point, the material thickness is small in order to minimize conversions. The total thickness to pass through the HBD is $0.024X_0$, and the thickness before the GEM pads is $0.007X_0$.

The Čerenkov light generated by electrons is directly collected on a photosensitive cathode plane, forming an almost circular spot image. The readout pad plane comprises hexagonal pads with an area of 6.2 cm^2 (hexagon side length $a = 1.55$ cm), which is comparable to, but smaller than, the spot size which has a maximum area of 9.9 cm^2.

The HBD is located in a field free region that preserves the original direction of the e^+e^- pair. The Čerenkov spots created by electron pairs with a small opening angle overlap, and therefore generate a signal in the HBD with twice the amplitude of a single electron. Electrons originating from π^0 and η Dalitz decays and γ conversions can largely be eliminated by rejecting tracks which correspond to large signals in the HBD.

III. HEAVY FLAVOR ELECTRON ANALYSIS

With the improved signal purity from the HBD, the double helicity asymmetry of the heavy flavor electrons was measured. In this section, we explain how the heavy flavor electron analysis and the purification of the heavy flavor electron sample using the HBD was performed.

A. Data set

The data used here were recorded by PHENIX during 2009. The data set was selected by a level-1 electron trigger in coincidence with the MB trigger. The electron trigger required a minimum energy deposit of 0.6 GeV in a 2×2 tile of towers in EMCal, Čerenkov light detection in the RICH and acceptance matching of these two hits. After a vertex cut of $|z_{vtx}| < 20$ cm and data quality cuts, an

equivalent of 1.4×10^{11} MB events, corresponding to 6.1 pb^{-1}, sampled by the electron trigger were analyzed.

B. Electron selection

Electrons are reconstructed using the detectors in the PHENIX central arm described above. Several useful variables for the electron selection which were used in the previous electron analysis in 2006 [25] are also used in this analysis. In addition to the conventional parameters, we introduced a new value, q_{clus}, for the HBD analysis.

q_{clus} Total charge of the associated HBD cluster calibrated in units of the number of photoelectrons (p.e.).

The electron selection cuts (eID cut) are listed in Table I. These cuts require hits in the HBD, RICH and EMCal that are associated with projections of the track onto these detectors. The shower profile in the EMCal is required to match the profile expected of an electromagnetic shower. For electrons, the energy deposit on EMCal, E, and the magnitude of the reconstructed momentum on DC and PC, p, should match due to their small mass. Therefore, the ratio, E/p, was required to be close to 1. Since the energy resolution of the EMCal depends on the momentum of the electron, the cut boundaries were changed in different momentum ranges. Charged particles traversing the CF_4 volume in the HBD produce also scintillation light, which has no directivity and creates hits with small charge in random locations in the GEM pads. To remove HBD background hits by the scintillation light, a minimum charge and a minimum cluster size were required for the HBD hit clusters. During this measurement, the efficiency for the Čerenkov light in one HBD sector was low compared with other sectors. Hence, we apply a different charge cut to that HBD sector for the electron selection.

TABLE I. eID cuts and nonphotonic electron cuts used in the electron analysis.

Electron ID cut
4.0σ matching between track and EMCal cluster
# of hit tubes in RICH around track ≥ 2
3.5σ matching between track and HBD cluster
shower profile cut on EMCal
$0.57 < E/p < 1.37$ ($0.5\ \text{GeV}/c < p_T < 1.0\ \text{GeV}/c$)
$0.60 < E/p < 1.32$ ($1.0\ \text{GeV}/c < p_T < 1.5\ \text{GeV}/c$)
$0.64 < E/p < 1.28$ ($1.5\ \text{GeV}/c < p_T < 5.0\ \text{GeV}/c$)
# of hit pads in HBD cluster ≥ 2
$q_{\text{clus}} > 8.0$ p.e.
($q_{\text{clus}} > 4.0$ p.e. for one low-gain HBD sector)

Nonphotonic electron cut
$8.0 < q_{\text{clus}} < 28.0$ p.e.
($4.0 < q_{\text{clus}} < 17.0$ p.e. for one low-gain HBD sector)

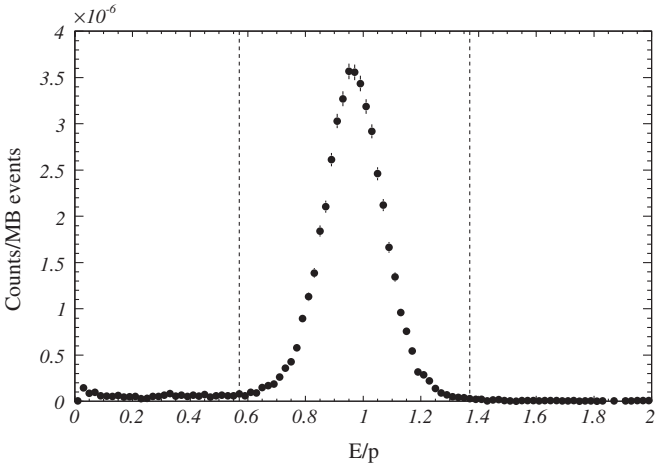

FIG. 3. E/p distributions for $0.5\ \text{GeV}/c < p_T < 1.0\ \text{GeV}/c$ reconstructed charged tracks with the eID cut other than the E/p cut. Criteria of the E/p cut for the momentum region are shown by dashed lines in the plot.

The E/p distribution for tracks selected with these cuts is shown in Fig. 3. The clear peak around $E/p = 1$ corresponds to electrons and the spread of events around the peak consists mainly of electrons from K_{e3} decays and misidentified hadrons. As the figure shows, the fraction of these background tracks in the reconstructed electron sample after applying eID cut including the E/p cut was small.

We remove the photonic electrons and purify the heavy flavor electrons on the basis of the associated HBD cluster charge. The nonphotonic electron cuts (npe cut) are also listed in Table I.

C. Yield estimation of heavy flavor electrons with the HBD

We categorize the HBD hit clusters into three types according to the source of the cluster. A cluster created by a single spot of Čerenkov light from a nonphotonic electron as shown in Fig. 4(a) is defined as a *single cluster*. On the other hand, a cluster created by merging spots of Čerenkov light from a track pair of photonic electrons as shown in Fig. 4(b) is defined as a *merging cluster*. However, a portion of the photonic electrons which have a large enough opening angle such that the two clusters do not merge (typically $\gtrsim 0.1$ rad) creates two separated single clusters as shown in Fig. 4(c). Therefore, the single clusters are created by both the nonphotonic electron and the photonic electron with a large opening angle.

We also define another type of cluster created by scintillation light, which we call a *scintillation cluster*. Scintillation hits which accidentally have large hit charges and have neighboring hits can constitute clusters. Photonic electrons from γ conversions after the HBD GEM pads do not create Čerenkov light in the HBD gas volume. Hence, they basically do not have associated clusters in the HBD,

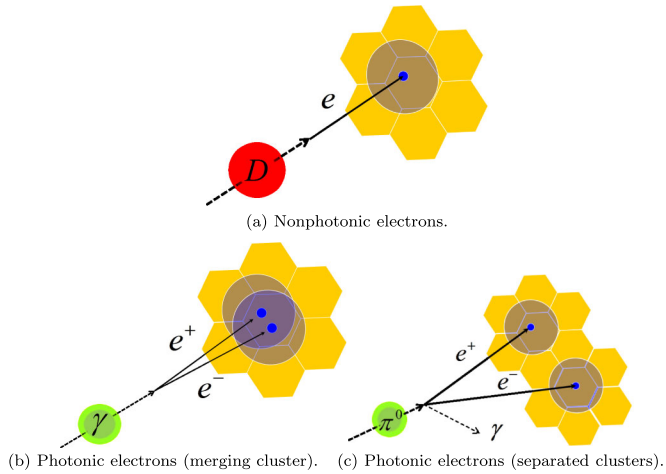

(a) Nonphotonic electrons.

(b) Photonic electrons (merging cluster). (c) Photonic electrons (separated clusters).

FIG. 4 (color online). Responses of the HBD for (a) nonphotonic electrons and (b,c) photonic electrons. (b) Most of the photonic electron pairs create merging clusters. (c) However, the photonic electrons with large opening angles create separated clusters.

and they are rejected by the HBD hit requirement in the eID cut. However, a portion of these are accidentally associated with scintillation clusters and satisfy the eID cut and so also survive in the reconstructed electron sample.

1. Yield estimation of single clusters

All clusters associated with the reconstructed electrons can be classified into the above three types. The yield of the electrons associated with the single clusters must be evaluated to estimate the yield of the heavy flavor electrons. The shapes of the $q_{\rm clus}$ distributions for the three cluster types are quite different since merging clusters have on average double the charge of single clusters, and the charge of scintillation clusters is considerably smaller than the charge of the single cluster. Using the difference in the shapes, we estimate yields of these clusters as follows.

The probability distributions of $q_{\rm clus}$ for single and merging clusters were estimated by using low-mass unlike-sign electron pairs reconstructed with only the eID cut, which is dominated by photonic electron pairs. We defined the unlike-sign electron pairs whose two electrons were associated with two different HBD clusters as separated electron pairs and the pairs whose two electrons were associated to the same HBD cluster as merging electron pairs. The probability distribution of $q_{\rm clus}$ for the single clusters were estimated by the $q_{\rm clus}$ distribution of the separated electron pairs, and the probability distribution of $q_{\rm clus}$ for the merging clusters was estimated by the $q_{\rm clus}$ distribution of the merging electron pairs. The reconstruction of the electron pairs creates a small bias on the shapes of the $q_{\rm clus}$ distributions. Corrections for this bias are estimated by simulation and applied to the distributions. The probability distributions are denoted as $f_{\rm c}^{\rm s}(q_{\rm clus})$ for the single clusters and $f_{\rm c}^{\rm m}(q_{\rm clus})$ for the merging clusters. The probability distribution of $q_{\rm clus}$ for the scintillation clusters is also estimated by the distribution of the hadron tracks reconstructed by the DC/PC tracking and the RICH veto and denoted as $f_{\rm c}^{\rm sci}(q_{\rm clus})$. Table II lists the variables used in the $q_{\rm clus}$ analysis.

The $q_{\rm clus}$ distribution of the reconstructed electrons found by applying the eID cut is fitted with a superposition of the three probability distributions

$$n_{\rm s} \times f_{\rm c}^{\rm s}(q_{\rm clus}) + n_{\rm m} \times f_{\rm c}^{\rm m}(q_{\rm clus}) + n_{\rm sci} \times f_{\rm c}^{\rm sci}(q_{\rm clus}), \qquad (4)$$

where $n_{\rm s}$, $n_{\rm m}$ and $n_{\rm sci}$ are fitting parameters that represent, respectively, the numbers of the reconstructed electrons associating to single clusters, merging clusters and scintillation clusters after applying the eID cut. The fraction of nonphotonic electrons and photonic electrons are different in different p_T regions of the reconstructed electron sample. Therefore, the fitting was performed for each p_T region, and $n_{\rm s}(p_T)$, $n_{\rm m}(p_T)$ and $n_{\rm sci}(p_T)$ for each p_T region were determined. In the fitting, the distribution functions, $f_{\rm c}^{\rm s}(q_{\rm clus})$, $f_{\rm c}^{\rm m}(q_{\rm clus})$ and $f_{\rm c}^{\rm sci}(q_{\rm clus})$ are assumed to be p_T independent because the velocity of electrons in the p_T region of interest is close enough to the speed of light in vacuum such that the yield of Čerenkov light from the electron is nearly independent of p_T. We also compared the shapes of the distributions in different p_T regions to confirm that the effect from the track curvature is small enough to be ignored even at $p_T \sim 0.5$ GeV/c. On the other hand, the distributions $f_{\rm c}^{\rm s}(q_{\rm clus})$, $f_{\rm c}^{\rm m}(q_{\rm clus})$ and $f_{\rm c}^{\rm sci}(q_{\rm clus})$ vary by

TABLE II. Summary of variables used in $q_{\rm clus}$ analysis.

Variable	Description
$f_{\rm c}^{\rm s}$	Probability distribution of $q_{\rm clus}$ for the single clusters
$f_{\rm c}^{\rm m}$	Probability distribution of $q_{\rm clus}$ for the merging clusters
$f_{\rm c}^{\rm sci}$	Probability distribution of $q_{\rm clus}$ for the scintillation clusters
$n_{\rm s}$	Number of single clusters after applying the eID cut
$n_{\rm m}$	Number of merging clusters after applying the eID cut
$n_{\rm sci}$	Number of scintillation clusters after applying the eID cut
$\tilde{n}_{\rm s}$	Number of single clusters after applying the eID cut and the npe cut
$\tilde{n}_{\rm m}$	Number of merging clusters after applying the eID cut and the npe cut
$\tilde{n}_{\rm sci}$	Number of scintillation clusters after applying the eID cut and the npe cut

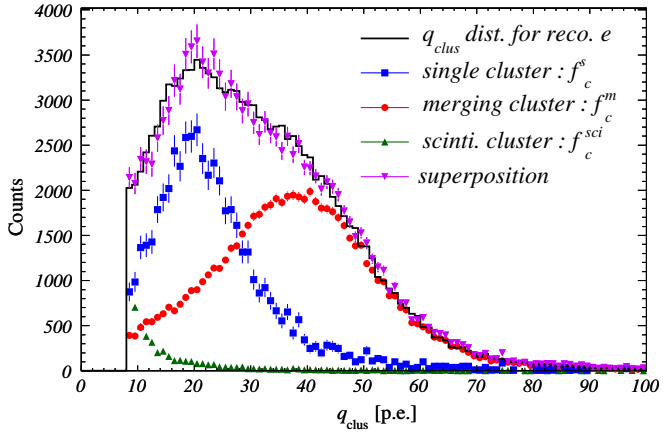

FIG. 5 (color online). Charge distribution of HBD clusters associated with reconstructed electrons with a transverse momentum ranging from 0.75 GeV/c to 1.00 GeV/c (solid black line) and the charge distribution for each component, i.e., single clusters ($n_s f_c^s$, blue circles), merging clusters ($n_m f_c^m$, red squares) and scintillation clusters ($n_{sci} f_c^{sci}$, green triangles). The superposition of these components is also shown (purple inverted triangles).

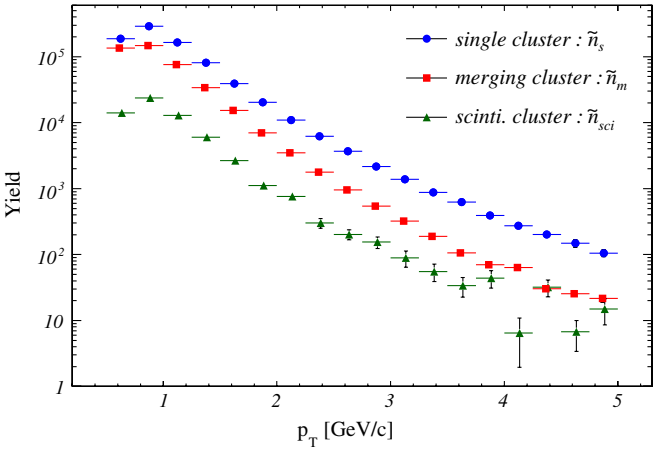

FIG. 6 (color online). Yield spectra of HBD clusters after applying the eID cut and the npe cut estimated from the HBD cluster charge fitting. The plot shows the spectrum for the single clusters ($\tilde{n}_s$, blue circle), the spectrum for the merging clusters ($\tilde{n}_m$, red square) and the spectrum for the scintillation clusters ($\tilde{n}_{sci}$, green triangle). The error bars represent fitting uncertainties.

about 10% between HBD sectors with nominal gain, and fitting is performed for each sector individually to account for this variation. The single low-gain sector exhibits a larger variation and is fitted separately.

The q_{clus} distribution for the reconstructed electrons with p_T ranging from 0.75 GeV/c to 1.00 GeV/c and the fitting result are shown in Fig. 5 for one HBD sector. The charge distribution of the reconstructed electrons is well reproduced by the superposition of the three individual components.

The total number of reconstructed electrons after applying both the eID cut and the npe cut for the three cluster types, which are represented as $\tilde{n}_s$, $\tilde{n}_m$ and $\tilde{n}_{sci}$, are calculated by applying the npe cut efficiencies of $\int_{q_{min}}^{q_{max}} dq f_c^s(q)$, $\int_{q_{min}}^{q_{max}} dq f_c^m(q)$ and $\int_{q_{min}}^{q_{max}} dq f_c^{sci}(q)$ to the fit results, n_s, n_m and n_{sci}, respectively. In the integrals, q_{min} and q_{max} represent the HBD charge boundaries in the npe cut of 8 p.e. and 28 p.e. (4 p.e. and 17 p.e. for the low-gain sector). The variables, $\tilde{n}$, are also summarized in Table II. Figure 6 shows the yield spectra from the calculation as functions of p_T.

2. Yield estimation of separated photonic electrons

The estimated $\tilde{n}_s$ is the sum of nonphotonic electrons and photonic electrons which create the separated clusters in the HBD. In the following description, we denote the photonic electrons which create merging clusters as *merging photonic electrons* (MPE) and those which create separated single clusters as *separated photonic electrons* (SPE). In this section, the number of SPE is estimated to obtain the yield of the nonphotonic electrons.

In the case where a reconstructed electron track is identified as an SPE, the partner electron generates an additional signal in the HBD, as illustrated in Fig. 4(c). This property is utilized to estimate the number of SPE. For this estimation, we defined a new value, q_{ring}:

q_{ring} The total charge in the HBD pads centered on a half of an annular region with an inner radius of 7.0 cm and an outer radius of 8.0 cm around the track projection of HBD as shown in Fig. 7. To avoid inefficient regions around the edges of the HBD sectors, we use one half of an annular region oriented away from the nearest sector edge (see Fig. 7). The q_{ring} value is normalized by the area of the half of the annular region in the definition.

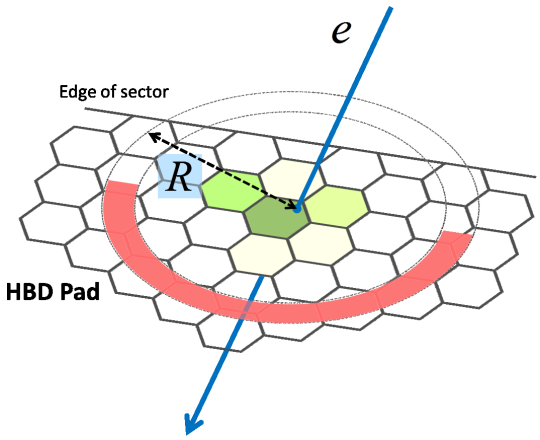

FIG. 7 (color online). A half of an annular region around the reconstructed electron track on the HBD for the definition of q_{ring}. The inner and outer radii of the annular region are 7.0 cm and 8.0 cm, respectively. The direction of the half region is determined as the opposite side to the edge of the HBD sector to avoid inefficiency around the edge.

TABLE III. Summary of variables used in $q_{\rm ring}$ analysis.

Variable	Description
$f_{\rm r}^{\rm spe}$	Probability distribution of $q_{\rm ring}$ for SPE
$f_{\rm r}^{\rm non\text{-}spe}$	Probability distribution of $q_{\rm ring}$ for nonphotonic electrons and MPE
$n_{\rm spe}$	Number of SPE after applying the eID cut and the npe cut
$n_{\rm non\text{-}spe}$	Number of electrons other than SPE after applying the eID cut and the npe cut

The choice of 7.0 cm to 8.0 cm is determined by three factors: (1) the distribution of the distance between separated clusters of SPE has a maximum around 7.0 cm, (2) few HBD clusters have radii larger than 7.0 cm and (3) a larger area includes more scintillation background and decreases the signal-to-background ratio. Whereas the $q_{\rm ring}$ distributions for the nonphotonic electrons and MPE comprise signals only from scintillation light, the distributions for SPE include the correlated signals around the tracks in addition to scintillation light. Table III lists the variables used in the $q_{\rm ring}$ analysis.

The $f_{\rm r}^{\rm spe}(q_{\rm ring})$ for SPE and the $f_{\rm r}^{\rm non\text{-}spe}(q_{\rm ring})$ for nonphotonic electrons and MPE can be estimated by hadron tracks and electron tracks with large $q_{\rm clus}$ values, which consist almost entirely of MPE. Because hadrons and MPE clusters do not create any correlated signals around their tracks, the $q_{\rm ring}$ distributions of the tracks are created by only the scintillation light.

The $f_{\rm r}^{\rm spe}(q_{\rm ring})$ was estimated by using simulations. The dominant photonic electrons come from the Dalitz decays of π^0 and η and γ from their decays which convert in materials. We simulated the detector responses for the Dalitz decay and the γ conversion events of the neutral mesons by a GEANT3 simulation [35] configured for the PHENIX detector system. The π^0 and η spectra were parametrized in the simulation by m_T-scaled Tsallis distributions [36], together with their known branching ratios to Dalitz decays and γ decays. In order to include contributions from scintillation light, $f_{\rm r}^{\rm non\text{-}spe}(q_{\rm ring})$, which is identical to the $q_{\rm ring}$ distribution from only the scintillation light, was convoluted to the result to obtain $f_{\rm r}^{\rm spe}(q_{\rm ring})$.

The $q_{\rm ring}$ distribution for the reconstructed electrons selected by applying the eID cut and the npe cut was fitted with the superposition of the $q_{\rm ring}$ distributions, $f_{\rm r}^{\rm spe}(q_{\rm ring})$ and $f_{\rm r}^{\rm non\text{-}spe}(q_{\rm ring})$, as

$$n_{\rm spe} \times f_{\rm r}^{\rm spe}(q_{\rm ring}) + n_{\rm non\text{-}spe} \times f_{\rm r}^{\rm non\text{-}spe}(q_{\rm ring}), \quad (5)$$

where $n_{\rm spe}$ and $n_{\rm non\text{-}spe}$ are fitting parameters and represent the numbers of SPE and other electrons in the $q_{\rm ring}$ distribution, respectively, as summarized above. Similar to the $q_{\rm clus}$ distribution, the fitting for the $q_{\rm ring}$ distribution was also performed for each electron p_T region and each HBD sector. Figure 8 shows a fitting result in one HBD sector in the electron p_T region from 0.75 GeV/c to 1.00 GeV/c.

3. Yield estimation of heavy flavor electrons

Using the above fitting results of $\tilde{n}_{\rm s}$ and $n_{\rm spe}$, the yield of nonphotonic electrons, $N^{\rm npe}$ was estimated with the formula

$$N^{\rm npe}(p_T) = \tilde{n}_{\rm s}(p_T) - n_{\rm spe}(p_T). \quad (6)$$

The remaining background for the heavy flavor electrons in the nonphotonic electron sample comes from K_{e3} decays and e^+e^- decays of light vector mesons, namely, ρ, ω, and ϕ. Electrons from the Drell-Yan process also contribute to the background; however, the contribution is known to be less than 0.5% of total heavy flavor electrons in this p_T range and can be ignored. We determined the yield of the heavy flavor electrons from $N^{\rm npe}$ by subtracting the components of the K_{e3} electrons, which are estimated by simulation using a measured K cross section [36], and the electrons from light vector mesons (LVM), which are already estimated in previously published result [24], as

$$N^{\rm HFe}(p_T) = N^{\rm npe}(p_T) - N^{Ke3}(p_T) - N^{\rm LVM}(p_T), \quad (7)$$

where $N^{Ke3}(p_T)$ and $N^{\rm LVM}(p_T)$ represent the electrons from the K_{e3} decays and the light vector meson decays, respectively.

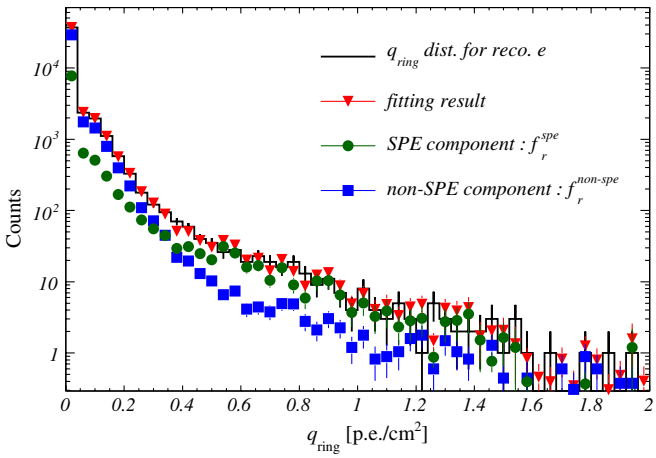

FIG. 8 (color online). HBD charge distribution in the annular region for the reconstructed electrons with a transverse momentum ranging from 0.75 GeV/c to 1.00 GeV/c (solid black line), the fitting result of the charge distribution for electrons with correlated charges ($n_{\rm spe} f_{\rm r}^{\rm spe}$, green circle) and without correlated charges ($n_{\rm non\text{-}spe} f_{\rm r}^{\rm non\text{-}spe}$, blue square) and the superposition of the fitting results (red inverted triangle).

D. Systematic uncertainty

The systematic uncertainties for the heavy flavor electron yield come from the fits for the $q_{\rm clus}$ distribution and the $q_{\rm ring}$ distribution and from estimations of K_{e3} contribution and misidentified hadrons.

The most significant source in these contributions is the fitting uncertainty for the $q_{\rm ring}$ distribution. We varied the radius of the annular region to an inner radius of 6.0 cm and an outer radius of 7.0 cm and also to 8.0 cm and 9.0 cm from the default radii of 7.0 cm and 8.0 cm. The uncertainty from the fitting was set to the amount of variation in $n_{\rm spe}$ after these changes. The estimated uncertainties decrease from about 16% of the heavy flavor electron yield in the momentum range of $0.50 < p_T < 1.00$ GeV/c to about 2% above 1.75 GeV/c.

The fitting uncertainty for the $q_{\rm clus}$ distribution comes from the estimation of the bias in the charge distribution shape due to the electron pair reconstruction. The systematic uncertainty from this effect is estimated to be less than 2% by simulation.

In the low momentum region, $0.50 < p_T < 1.00$ GeV/c, uncertainties from the K_{e3} contribution and the hadron misreconstruction are significant. The uncertainty from the K_{e3} contribution comes almost entirely from the uncertainty on the K cross section used in the K_{e3} simulation. This uncertainty amounts to about 4% of the total heavy flavor electron yield in the low momentum region and decreases to less than 1% for $p_T > 0.75$ GeV/c. We also estimated the upper limits of the hadron contamination due to misreconstructions employing a hadron-enhanced event set. As a result, we determined the upper limits as 4% of the total heavy flavor electron yield in the low momentum region which decreases to less than 1% over 1.5 GeV/c. The upper limits are assigned as the systematic uncertainties from hadron misreconstructions. Table IV summarizes the systematic uncertainties on the heavy flavor electron yield.

E. Results of heavy flavor electron yield and signal purity

From Eqs. (6) and (7) and the discussion in Sec. III D, the heavy flavor electron yield spectrum with the systematic uncertainties was determined. The spectrum is shown in Fig. 9. We also show the yield of inclusive reconstructed electrons after applying the eID cut and the npe cut and the estimated K_{e3} contribution. The electrons from e^+e^- decays of the light vector mesons are not shown in Fig. 9, but they are less than 5% of the heavy flavor electron yield in this p_T range.

The ratio of the nonphotonic electron yield to the photonic electron yield in this measurement,

$$R(p_T) \equiv \frac{N^{\rm npe}(p_T)}{N_e^{\rm reco}(p_T) - N^{\rm npe}(p_T)}, \tag{8}$$

where $N_e^{\rm reco}$ denotes the total number of reconstructed electrons after applying the eID cut and the npe cut, is shown in the top panel of Fig. 10. In Eq. (8), we assumed the fraction of misidentified hadrons in the reconstructed electrons after the cuts is negligible as shown in Fig. 3, and so the number of photonic electrons can be represented as $N_e^{\rm reco}(p_T) - N^{\rm npe}(p_T)$. The same ratio from a previous measurement [24] is also shown in the figure. The previous measurement employed two other methods for the background estimation, namely, a cocktail method and a converter method. In the cocktail method, a sum of electron spectra from various background sources was calculated using a Monte Carlo hadron decay generator. This sum was subtracted from the inclusive electron sample to isolate the heavy flavor contribution. With the converter method, a photon converter around the beam pipe was introduced to increase the photon conversion probability by a well-defined amount and thus allow determination of the

TABLE IV. Relative systematic uncertainties given on the heavy flavor electron yield.

Source	Uncertainty	p_T range (GeV/c)
$q_{\rm ring}$ fitting	16%	$(0.50 < p_T < 0.75)$
	6% ~ 4%	$(0.75 < p_T < 1.75)$
	2%	$(1.75 < p_T)$
$q_{\rm clus}$ fitting	2%	$(0.50 < p_T < 0.75)$
	<1%	$(0.75 < p_T)$
K_{e3}	4%	$(0.50 < p_T < 0.75)$
	<1%	$(0.75 < p_T)$
Hadron misidentified	4%	$(0.50 < p_T < 0.75)$
	<1%	$(0.75 < p_T)$

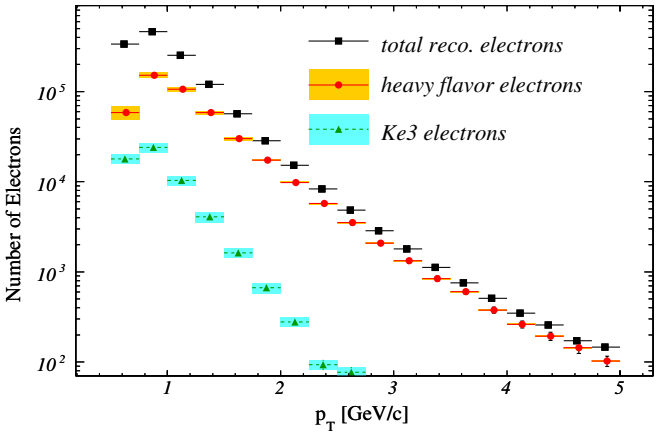

FIG. 9 (color online). Heavy flavor electron yield spectrum. The black square points represent the total number of the reconstructed electrons after applying the eID cut and the npe cut. The red circle points represent the estimated yield of the heavy flavor electrons. The yellow bands represent the systematic uncertainties for the heavy flavor electron yield. The green triangle points with dashed lines represent the estimated K_{e3} contribution with systematic uncertainties shown by light-blue bands.

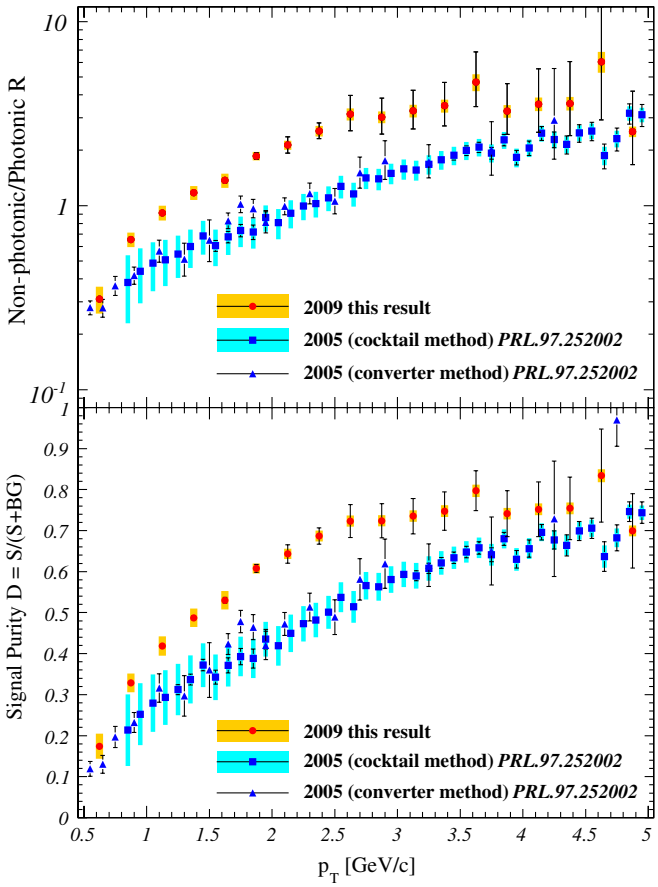

FIG. 10 (color online). (top) Ratio between the yields of the nonphotonic electrons and the photonic electrons in the reconstructed tracks. The red circles and the blue squares and triangles represent this analysis result and the previous result [24], respectively. The error bars and bands represent the statistic and the systematic uncertainties. (bottom) Signal purity, which is a ratio of the yield of the heavy flavor electrons to the total reconstructed electrons.

photonic background. The nonphotonic to photonic electron ratio is improved by a factor of about 2 or more in $p_T > 1.0$ GeV/c compared with the previously measured result due to the rejection of photonic electrons by the HBD.

The signal purity is defined as the ratio of the yield of the heavy flavor electrons to the reconstructed electrons after applying the eID cut and the npe cut,

$$D(p_T) \equiv \frac{N^{\mathrm{HFe}}(p_T)}{N_e^{\mathrm{reco}}(p_T)}. \tag{9}$$

The result is shown as the bottom plot in Fig. 10. We also show the result of the signal purity in the previous measurement. Comparing with the previously measured result, the signal purity is improved by a factor of about 1.5 in a p_T range from 0.75 GeV/c to 2.00 GeV/c.

IV. HEAVY FLAVOR ELECTRON CROSS SECTION

The invariant cross section is calculated from

$$E\frac{d^3\sigma}{dp^3} = \frac{1}{2\pi p_T}\frac{1}{L}\frac{1}{A\epsilon_{\mathrm{rec}}\epsilon_{\mathrm{trig}}}\frac{N(\Delta p_T, \Delta y)}{\Delta p_T \Delta y}, \tag{10}$$

where L denotes the integrated luminosity, A the acceptance, ϵ_{rec} the reconstruction efficiency, ϵ_{trig} the trigger efficiency and N the estimated number of heavy flavor electrons.

The luminosity, L, was calculated from the number of MB events divided by the cross section for the MB trigger. For the latter, a value of 23.0 mb with a systematic uncertainty of 9.6% was estimated from van-der-Meer scan results [37] corrected for the relative changes in the BBC performance. The combination of the acceptance and the reconstruction efficiency, $A\epsilon_{\mathrm{rec}}(p_T)$, was estimated by a GEANT3 simulation. We found that $A\epsilon_{\mathrm{rec}}(p_T)$ has a value of $4.7\% \times (1 \pm 8 \times 10^{-2}(\mathrm{acc}) \pm 6 \times 10^{-2}(\mathrm{rec}))$, with a slight p_T dependence.

The efficiency of the MB trigger for the hard scattering processes, including heavy flavor electron production, is $\epsilon_{\mathrm{trig}}^{\mathrm{MB}} = 79.5\% \times (1 \pm 2.5 \times 10^{-2})$. The efficiency of the electron trigger for the electrons under the condition of the MB trigger firing, $\epsilon_{\mathrm{trig}}^{e|\mathrm{MB}}(p_T) \equiv \epsilon_{\mathrm{trig}}(p_T)/\epsilon_{\mathrm{trig}}^{\mathrm{MB}}$, can be calculated by the ratio of the number of the reconstructed electrons in the MB triggered sample in coincidence with the electron trigger to the number of the reconstructed electrons without the coincidence. The efficiency $\epsilon_{\mathrm{trig}}^{e|\mathrm{MB}}$ is shown in Fig. 11 as a function of p_T. Whereas we used the calculated efficiency values for the momentum region of $p_T < 1.25$ GeV/c, we assumed a saturated efficiency for $p_T > 1.25$ GeV/c and estimated the value with a fitting as

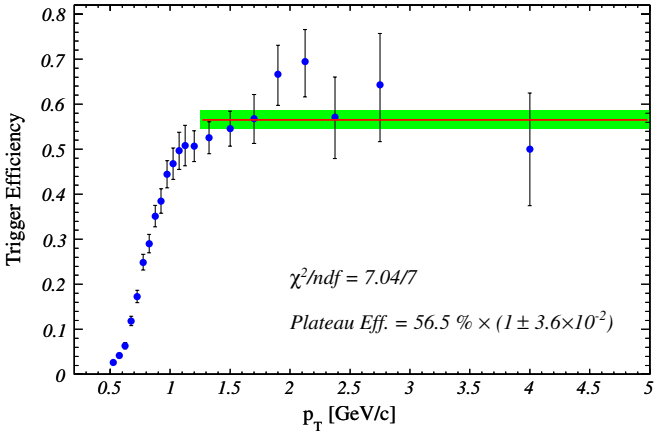

FIG. 11 (color online). Efficiency of the electron trigger for reconstructed electrons under the condition that the MB trigger was issued. The red line represents the fitting result with the constant function, and the green band represents the fitting uncertainty.

TABLE V. Relative systematic uncertainties on the cross section due to uncertainties in the total sampled luminosity, trigger efficiencies and detector acceptance. These systematic uncertainties are globally correlated in all p_T regions except $p_T < 1.25$ GeV/c for the uncertainties on $\epsilon_{\rm trig}^{e|{\rm MB}}$.

Source	Uncertainty	p_T range (GeV/c)
MB trig. cross section	9.6%	
Acceptance A	8%	
Rec. efficiency $\epsilon_{\rm rec}$	6%	
MB trig. efficiency $\epsilon_{\rm trig}^{\rm MB}$	2.5%	
e trig. efficiency $\epsilon_{\rm trig}^{e|{\rm MB}}$	~4%	$0.50 < p_T < 1.25$
	3.6%	$1.25 < p_T$

shown in Fig. 11. The fitting result is $\epsilon_{\rm plateau} = 56.5\% \times (1 \pm 3.6 \times 10^{-2})$. The systematic uncertainty of $\epsilon_{\rm trig}^{e|{\rm MB}}$ was assigned to be $\Delta\epsilon/\epsilon \sim 4\%$ for $p_T < 1.25$ GeV/c, which was estimated from the statistical uncertainty in the efficiency calculation and 3.6% for $p_T > 1.25$ GeV/c from the fitting uncertainty. The total trigger efficiency $\epsilon_{\rm trig}(p_T)$ can be calculated with the above two efficiencies as $\epsilon_{\rm trig}(p_T) = \epsilon_{\rm trig}^{\rm MB} \times \epsilon_{\rm trig}^{e|{\rm MB}}(p_T)$. Table V summarizes the systematic uncertainties on the cross section due to uncertainties in the total sampled luminosity, trigger efficiencies and detector acceptance. All systematic uncertainties listed in Table V are globally correlated over whole p_T region ($p_T > 1.25$ GeV/c for the uncertainties on $\epsilon_{\rm trig}^{e|{\rm MB}}$).

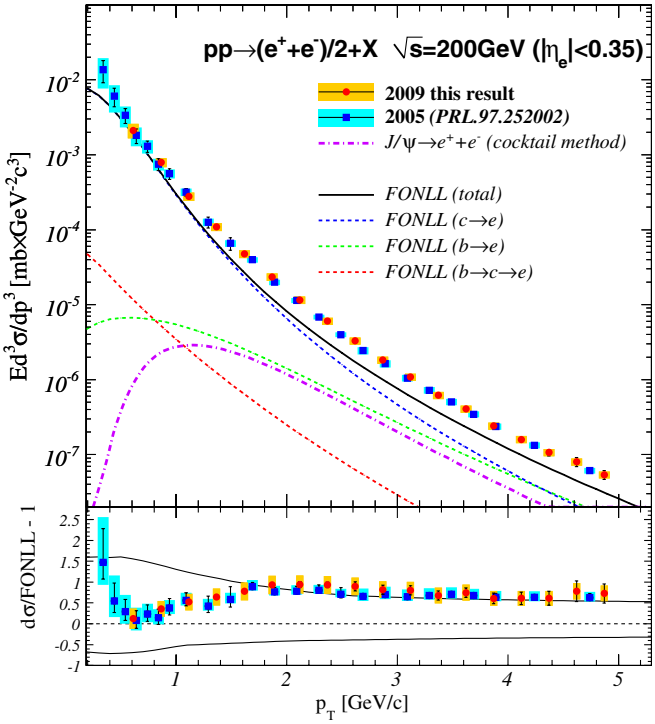

FIG. 12 (color online). (top) Invariant differential cross sections of electrons from heavy-flavor decays. The red circles are this analysis of 2009 data, and the blue squares are the previous 2005 data [24] for the nonphotonic electron cross sections. The error bars and bands represent the statistical and systematic uncertainties. The scaling uncertainty from the van-der-Meer scan is not included in the error bands because the same uncertainty must be considered for both the results of 2009 and 2005. The purple dashed-dotted line is the electron cross section from $J/\psi \to e^+ + e^-$ decays estimated from the cocktail method [25]. The solid and dashed curves are the FONLL calculations. (bottom) Difference of the ratio of the data and the FONLL calculation from 1. The upper and lower curve shows the theoretical upper and lower limit of the FONLL calculation.

The measured cross section of heavy flavor electrons is shown in Fig. 12 and tabulated in Table VI. A correction for bin width [38] is applied to the p_T value of each point. The figure also shows the previously published result [24]. The new result agrees well with the previous result within the uncertainties. Note that in this paper, we employed a new analysis method with the HBD, whereas the previous measurement employed different methods, namely, the cocktail method and the converter method. The consistency between these measurements proves that additional photonic backgrounds generated in the HBD material are removed, and that this new analysis method with the HBD is robust.

The electron cross section from $J/\psi \to e^+ + e^-$ decays estimated by the cocktail method [25] and a fixed-order next-to-leading-log (FONLL) pQCD calculation of the heavy flavor contributions to the electron spectrum [39] are also shown in Fig. 12. The J/ψ contribution to the heavy flavor electrons is less than 2% in $p_T < 1.25$ GeV/c and increase to ~20% until $p_T = 5.0$ GeV/c. The FONLL pQCD calculation shows that the heavy flavor electrons in

TABLE VI. Data table for the cross section result corresponding to Fig. 12.

p_T [GeV/c]	$E\frac{d^3\sigma}{dp^3}$	Stat. error [mb × GeV$^{-2}c^3$]	Syst. error
0.612	2.12×10^{-3}	0.04×10^{-3}	0.47×10^{-3}
0.864	7.93×10^{-4}	0.09×10^{-4}	1.11×10^{-4}
1.115	2.78×10^{-4}	0.03×10^{-4}	0.37×10^{-4}
1.366	1.09×10^{-4}	0.02×10^{-4}	0.13×10^{-4}
1.617	4.77×10^{-5}	0.08×10^{-5}	0.58×10^{-5}
1.867	2.34×10^{-5}	0.05×10^{-5}	0.27×10^{-5}
2.118	1.15×10^{-5}	0.04×10^{-5}	0.13×10^{-5}
2.369	6.05×10^{-6}	0.20×10^{-6}	0.68×10^{-6}
2.619	3.28×10^{-6}	0.19×10^{-6}	0.37×10^{-6}
2.869	1.82×10^{-6}	0.11×10^{-6}	0.20×10^{-6}
3.120	1.08×10^{-6}	0.07×10^{-6}	0.12×10^{-6}
3.370	6.20×10^{-7}	0.41×10^{-7}	0.69×10^{-7}
3.620	4.07×10^{-7}	0.26×10^{-7}	0.45×10^{-7}
3.870	2.42×10^{-7}	0.19×10^{-7}	0.27×10^{-7}
4.121	1.59×10^{-7}	0.15×10^{-7}	0.18×10^{-7}
4.371	1.07×10^{-7}	0.11×10^{-7}	0.12×10^{-7}
4.621	8.02×10^{-8}	1.11×10^{-8}	0.89×10^{-8}
4.871	5.38×10^{-8}	0.71×10^{-8}	0.60×10^{-8}

the low momentum region are dominated by charm quark decays, and the contribution from bottom quarks in $p_T < 1.25$ GeV/c is less than 5%.

V. HEAVY FLAVOR ELECTRON SPIN ASYMMETRY

Since parity is conserved in QCD processes, thereby disallowing finite longitudinal single spin asymmetries, using Eq. (3), we express the expected electron yields for each beam-helicity combination as

$$\begin{aligned} N^{\rm exp}_{++}(N_0, A_{LL}) &= N_0(1 + |P_{\rm B}P_{\rm Y}|A_{LL}) \\ N^{\rm exp}_{--}(N_0, A_{LL}) &= N_0(1 + |P_{\rm B}P_{\rm Y}|A_{LL})/r_{--} \\ N^{\rm exp}_{+-}(N_0, A_{LL}) &= N_0(1 - |P_{\rm B}P_{\rm Y}|A_{LL})/r_{+-} \\ N^{\rm exp}_{-+}(N_0, A_{LL}) &= N_0(1 - |P_{\rm B}P_{\rm Y}|A_{LL})/r_{-+}, \end{aligned} \tag{11}$$

where $N^{\rm exp}_{\pm\pm}(N_0, A_{LL})$ denote the expected yields for collisions between the blue beam helicity ($\pm$) and the yellow beam helicity ($\pm$) and N_0 is the expected yield in collisions of unpolarized beams under the same integrated luminosity as the $++$ beam-helicity combination. $N^{\rm exp}_{\pm\pm}(N_0, A_{LL})$ are used for fitting functions to estimate A_{LL} as described below. $P_{\rm B}$ and $P_{\rm Y}$ represent the polarizations of the beams. The beam polarizations are measured with a carbon target polarimeter [40], normalized by the absolute polarization measured with a separate polarized atomic hydrogen jet polarimeter [41,42] at another collision point in RHIC ring. The measured polarizations are about $P = 57\%$ with a relative uncertainty of $\Delta P/P = 4.7 \times 10^{-2}$ in the measurement. The relative luminosities are defined as the ratio of the luminosities in the beam-helicity combinations,

$$r_{--} \equiv \frac{L_{++}}{L_{--}} \qquad r_{+-} \equiv \frac{L_{++}}{L_{+-}} \qquad r_{-+} \equiv \frac{L_{++}}{L_{-+}}, \tag{12}$$

where $L_{\pm\pm}$ represent the integrated luminosities in the beam-helicity combinations shown by the subscript. The relative luminosities are determined by the ratios of MB trigger counts in the four beam-helicity combinations.

The double-spin asymmetry for inclusive electrons after applying the eID cut and the npe cut, which include not only the heavy flavor electrons (S) but also the background electrons (BG), is determined by simultaneously fitting the yields of electrons in each of the four beam-helicity combinations with the expected values $N^{\rm exp}_{\pm\pm}(N_0, A_{LL})$ from Eq. (11), where A_{LL} and N_0 are free parameters. To perform the fit, a log likelihood method assuming Poisson distributions with expected values of $N^{\rm exp}_{\pm\pm}(N_0, A_{LL})$ was employed. The fit was performed for electron yields in each fill to obtain the fill-by-fill double-spin asymmetry. We confirmed that all asymmetries in different fills are consistent with each other within their statistical uncertainties, and, therefore, the patterns of the crossing helicities in the fills do not affect the asymmetry measurement.

TABLE VII. Systematic uncertainties by type. The scaling uncertainty denotes an uncertainty which scales the raw asymmetry $A_{LL}^{\rm S+BG}$, and the offset uncertainty denotes an uncertainty on the absolute value of the asymmetry. The "global" in this table means the uncertainties are globally correlated in all p_T regions. The scaling uncertainty is represented as the ratio of the uncertainty to the signal ($\Delta S/S$) given in percent, and the offset uncertainty is represented as the absolute value of the uncertainty.

Source	Uncertainty	Type
Signal purity D	~6%	Scaling
Polarization ($\frac{\Delta(P_B P_Y)}{P_B P_Y}$)	8.8%	Global scaling
Relative luminosity r	0.14×10^{-2}	Global offset
Background asymmetry A_{LL}^{BG}	$0.2 \times 10^{-2} \times \frac{1-D}{D}$	Offset

The final double-spin asymmetry for inclusive electrons, $A_{LL}^{\rm S+BG}(p_T)$, was calculated as the weighted mean of the fill-by-fill asymmetries.

The double-spin asymmetry in the heavy flavor electron production, $A_{LL}^{\rm HFe}$, was determined from

$$A_{LL}^{\rm HFe}(p_T) = \frac{1}{D(p_T)} A_{LL}^{\rm S+BG}(p_T) - \frac{1 - D(p_T)}{D(p_T)} A_{LL}^{\rm BG}(p_T), \tag{13}$$

where $A_{LL}^{\rm BG}$ represents the spin asymmetries for the background electron production, and D represents the signal purity defined in Eq. (9) and shown in Fig. 10. As previously discussed, most of the background electrons come from Dalitz decays of the π^0 and η or from conversions of photons from decays of those hadrons. The fractional contribution on the partonic level, and therefore the production mechanism for the π^0 and η, is expected to be very similar up to ~10 GeV/c [10,13]. We assume identical spectra for double-spin asymmetries of π^0 production and η

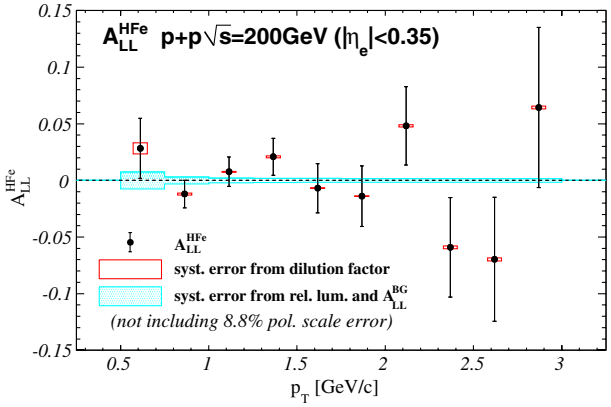

FIG. 13 (color online). Double-spin asymmetry of the heavy flavor electron production. The open-box (red) error bands represent scaling systematic uncertainties from the dilution factor, and the shaded-box (blue) error bands represents offset systematic uncertainties from relative luminosity and the background spin asymmetry.

TABLE VIII. Data table for the A_{LL}^{HFe} result corresponding to Fig. 13.

p_T [GeV/c]	A_{LL}^{HFe}	Stat. uncertainty	Syst. uncertainty (offset)	Syst. uncertainty (scale)
0.612	2.83×10^{-2}	2.66×10^{-2}	0.75×10^{-2}	0.50×10^{-2}
0.864	-1.20×10^{-2}	1.21×10^{-2}	0.30×10^{-2}	0.08×10^{-2}
1.115	0.76×10^{-2}	1.30×10^{-2}	0.21×10^{-2}	0.04×10^{-2}
1.366	2.08×10^{-2}	1.63×10^{-2}	0.18×10^{-2}	0.10×10^{-2}
1.617	-0.69×10^{-2}	2.18×10^{-2}	0.17×10^{-2}	0.03×10^{-2}
1.867	-1.39×10^{-2}	2.68×10^{-2}	0.16×10^{-2}	0.03×10^{-2}
2.118	4.82×10^{-2}	3.46×10^{-2}	0.16×10^{-2}	0.09×10^{-2}
2.369	-5.91×10^{-2}	4.40×10^{-2}	0.16×10^{-2}	0.11×10^{-2}
2.619	-6.97×10^{-2}	5.47×10^{-2}	0.16×10^{-2}	0.13×10^{-2}
2.869	6.43×10^{-2}	7.07×10^{-2}	0.16×10^{-2}	0.12×10^{-2}

production and estimated A_{LL}^{BG} from only the π^0 double-spin asymmetry using data from this PHENIX measurement. The resulting A_{LL}^{BG} is $-0.1 \times 10^{-2} < A_{LL}^{\mathrm{BG}} < 0.1 \times 10^{-2}$ in $0.5 < p_T < 2.5$ GeV/c and $0.1 \times 10^{-2} < A_{LL}^{\mathrm{BG}} < 0.2 \times 10^{-2}$ in $2.5 < p_T < 3.0$ GeV/c, with uncertainties less than 0.2×10^{-2}.

Systematic uncertainties on A_{LL}^{HFe} are separated into scaling uncertainties and offset uncertainties. The scaling uncertainties come from uncertainty in the beam polarizations, P_B and P_Y, and the signal purity, D. The uncertainty from the beam polarization is estimated as $\Delta(P_B P_Y)/P_B P_Y = 8.8\%$ which is globally correlated over the whole p_T range. The offset uncertainties come from uncertainties in the relative luminosity, r, and the background asymmetry, A_{LL}^{BG}. The uncertainty in the relative luminosity is globally correlated and is estimated by comparing the relative luminosities measured by the MB and ZDC triggers. This uncertainty is determined to be $\Delta r = 1.4 \times 10^{-3}$. The systematic uncertainties are summarized in Table VII.

A transverse double-spin asymmetry A_{TT}, which is defined by the same formula as Eq. (2) for the transverse polarizations, can contribute to A_{LL} through the residual transverse components of the beam polarizations. The product of the transverse components of the beam polarization is measured to be $\sim 10^{-2}$ in this experiment. For π^0 production, the A_{TT} is expected to be $\sim 10^{-4}$ based on an NLO QCD calculation [43]. If we assume the transverse asymmetries of π^0 and heavy flavor electrons are comparable, we arrive at the value of $A_{LL} \sim 10^{-6}$. This value is negligible compared with the precision of the $A_{LL}^{\mathrm{S+BG}}$ measurement of $\sim 10^{-3}$.

The result of the double-spin asymmetry of heavy flavor electrons is shown in Fig. 13 and tabulated in Table VIII. We show systematic uncertainties for scaling and offset separately in the figure. The measured asymmetry is consistent with zero.

VI. DISCUSSION

In this section, we discuss the constraint of Δg from the measured double-spin asymmetry. In $p + p$ collisions at $\sqrt{s} = 200$ GeV, heavy flavor electrons with momentum ranging $0.50 < p_T < 1.25$ GeV/c are mainly produced by open charm events. Open charm production is well described by pQCD calculations, which can be factorized into charm quark production at the partonic level and fragmentation of the charm quarks into charmed hadrons. Using polarized and unpolarized parton distribution functions (PDFs), the respective cross sections for charm quark production are determined. PYTHIA8 [44,45] simulations are then used to model the fragmentation and semileptonic decay processes. The spin asymmetry A_{LL}^{HFe} is the ratio of the polarized and unpolarized cross sections, and a comparison between the measured and calculated values of A_{LL}^{HFe} can thereby provide constraints on the gluon polarization Δg.

For this discussion, we calculated the charm quark cross section in the partonic level using a LO pQCD calculation [20]. In LO pQCD calculations, only $gg \to c\bar{c}$ and $q\bar{q} \to c\bar{c}$ are allowed for the open charm production. The charm quarks are primarily created by the gg interaction in the unpolarized hard scattering, and the $q\bar{q}$ contribution is known to be just a few percent in this momentum region [23]. In addition, the antiquark polarizations are known to be small from semi-inclusive deep inelasticc scattering measurements precisely enough that both deFlorian-Sassot-Stratmann-Vogelsang (DSSV) [19] and Glück-Reya-Stratmann-Vogelsang (GRSV) [46] expect contribution of polarized $q\bar{q}$ cross section to the double-spin asymmetry of the heavy flavor electrons in $|\eta| < 0.35$ and $p_T < 3.0$ GeV/c to be $\sim 10^{-4}$ [23], which is much smaller than the accuracy of this measurement. Therefore, in this analysis of Δg, we ignore the $q\bar{q}$ interaction and assume the asymmetries are due only to the gg interaction. Under the assumption, the spin asymmetry of the heavy flavor electrons is expected to be approximately proportional to the square of polarized gluon distribution normalized by the unpolarized distribution, $|\Delta g/g(x, \mu)|^2$.

To calculate the cross section of the $gg \to c\bar{c}$ process, CTEQ6M [47] was employed for the unpolarized PDF. For the polarized PDF, we assumed $|\Delta g(x, \mu)| = Cg(x, \mu)$ where C is a constant. The charm quark mass was assumed as $m_c = 1.4$ GeV/c^2, and the factorization

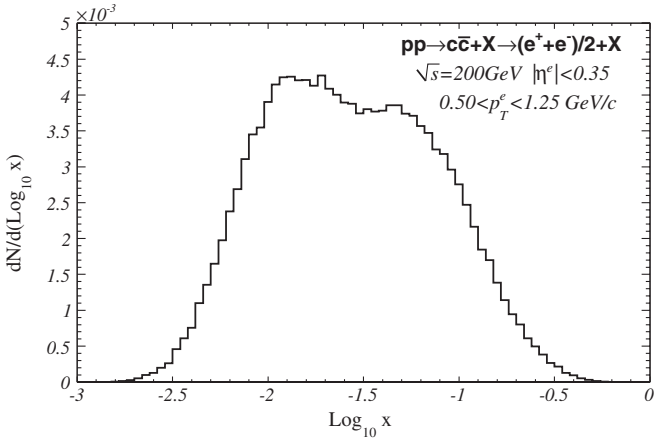

FIG. 14. Bjorken x distribution of gluons contributing the heavy flavor electron production with momentum ranging $0.50 < p_T < 1.25$ GeV/c obtained from PYTHIA simulation. The distribution is normalized with respect to the number of total generated charmed hadrons.

scale in CTEQ6 and the renormalization scale were assumed to be identical to $\mu = m_T^c \equiv \sqrt{p_T^{c2} + m_c^2}$.

The fragmentation and decay processes were simulated with a PYTHIA simulation. We generated $pp \to c\bar{c} + X$ events and selected electrons from the charmed hadrons, D^+, D^0, D_s, Λ_c and their antiparticles. We scaled the charm quark yield in PYTHIA with respect to the pQCD calculated unpolarized and polarized cross sections to obtain unpolarized and polarized electron yields from charmed hadron decays under these cross sections. We also applied a pseudorapidity cut of $|\eta| < 0.35$ for the electrons to match the acceptance of the PHENIX central arms. The shape of the expected spin asymmetry $A_{LL}^{\mathrm{HFe}}(p_T)$ is then determined from the simulated electron yields.

Figure 14 shows the distribution of the gluon Bjorken x contributing to heavy flavor electron production in the momentum range $0.50 < p_T < 1.25$ GeV/c from PYTHIA. Using the mean and the root-mean-square of the distribution for $0.50 < p_T < 1.25$ GeV/c, we determine the mean x for heavy flavor electron production to be $\langle \log_{10} x \rangle = -1.6^{+0.5}_{-0.4}$.

We calculated expected $A_{LL}^{\mathrm{HFe}}(p_T)$ by varying $C = |\Delta g/g|$. Figure 15(a) shows several of these curves, along with the measured points. χ^2 values are calculated for each value of C, along with related uncertainties. By assuming that the systematic uncertainties on the points are correlated and represent global shifts, we defined the quantity $\hat{\chi}^2$ as

$$\begin{aligned}
\hat{\chi}^2(C) &\equiv -2\log((2\pi)^{\frac{n}{2}}\hat{P}(C)) \\
\hat{P}(C) &\equiv \int dpdqN(p)N(q) \times \prod_{i=1}^{n} N\left(\frac{(y_i + p\epsilon^i_{\mathrm{syst}}{}^{\mathrm{offset}} - (1 + q\gamma^i_{\mathrm{syst}}{}^{\mathrm{scale}})f(x_i; C))}{\epsilon^i_{\mathrm{stat}}}\right) \\
\gamma^i_{\mathrm{syst}}{}^{\mathrm{scale}} &= \sqrt{\left(\frac{\epsilon^i_{\mathrm{syst}}{}^{\mathrm{scale}}}{y_i}\right)^2 + \left(\frac{\Delta(P_B P_Y)}{P_B P_Y}\right)^2},
\end{aligned} \tag{14}$$

where $N(X)$ denotes the normal probability distribution, i.e., $N(X) = 1/\sqrt{2\pi}\exp(-X^2/2)$, n is the number of the data points and equal to three, and for the ith data point, x_i is the p_T value, y_i is the A_{LL} value and $\epsilon^i_{\mathrm{stat}}$, $\epsilon^i_{\mathrm{syst}}{}^{\mathrm{offset}}$ and $\epsilon^i_{\mathrm{syst}}{}^{\mathrm{scale}}$ represent the statistical, offset systematic and scaling systematic uncertainties, respectively. $f(p_T; C)$ denotes the expected $A_{LL}(p_T)$ for the parameter of $C = |\Delta g/g|$. $\Delta(P_B P_Y)$ is an uncertainty for polarization. If we set the systematic uncertainties, $\epsilon^{\mathrm{offset}}_{\mathrm{syst}}$ and $\gamma^i_{\mathrm{syst}}{}^{\mathrm{scale}}$, to zero, the newly defined $\hat{\chi}^2$ is consistent with the conventional χ^2.

The resulting $\hat{\chi}^2$ curve is shown in Fig. 15(b), plotted as a function of $C^2 = |\Delta g/g|^2$ because the curvature becomes almost parabolic. The minimum of $\hat{\chi}^2$, $\hat{\chi}^2_{\mathrm{min}}$ is located at $|\Delta g/g|^2 = 0.0$ which is the boundary of $|\Delta g/g|^2$. $\Delta\hat{\chi}^2 \equiv \hat{\chi}^2 - \hat{\chi}^2_{\mathrm{min}} = 1$ and 9 were utilized to determine 1σ and 3σ uncertainties. With these criteria, we found the constraints on the gluon polarization are $|\Delta g/g(\langle \log_{10} x \rangle, \mu)|^2 < (3.0 \times 10^{-2}(1\sigma)$ and $10.0 \times 10^{-2}(3\sigma)$. The constraints are consistent with theoretical expectations for $\Delta g/g(x, \mu)$ at $\langle \log_{10} x \rangle = -1.6^{+0.5}_{-0.4}$ and $\mu = 1.4$ GeV which are ~ -0.006 from DSSV, ~ 0.016 from GRSV(standard) and ~ 0.019 from GRSV(value) using CTEQ6 [47] for the unpolarized PDF.

The effects of the charm quark mass and scale factor in the cross section calculation were also checked by varying the charm mass from $m_c = 1.3$ GeV/c^2 to 1.5 GeV/c^2 and the scale to $\mu^2 = 0.75 m_T^{c2}$ and $1.5 m_T^{c2}$. Figure 15(b) also shows the resulting $\hat{\chi}^2$ curves. Considering the variation of the crossing position at $\Delta\hat{\chi}^2 = 1$, the constraint including the uncertainties from the charm mass and the scale can be represented as $|\Delta g/g|^2 < (3.0^{+0.4}_{-0.2}(\mathrm{mass})^{+0.5}_{-0.3}(\mathrm{scale})) \times 10^{-2}$ (1σ).

The integral of the CTEQ6 unpolarized PDF in the sensitive x region of $\langle \log_{10} x \rangle = -1.6^{+0.5}_{-0.4}$ and $\mu = 1.4$ GeV is $\int_{0.01}^{0.08} dx g(x, \mu) = 4.9$. Hence, the constraint on the integral of the polarized PDF at 1σ corresponds to $|\int_{0.01}^{0.08} dx \Delta g(x, \mu)| < 0.85$. This study also highlights the possibility for constraining Δg in this Bjorken x region

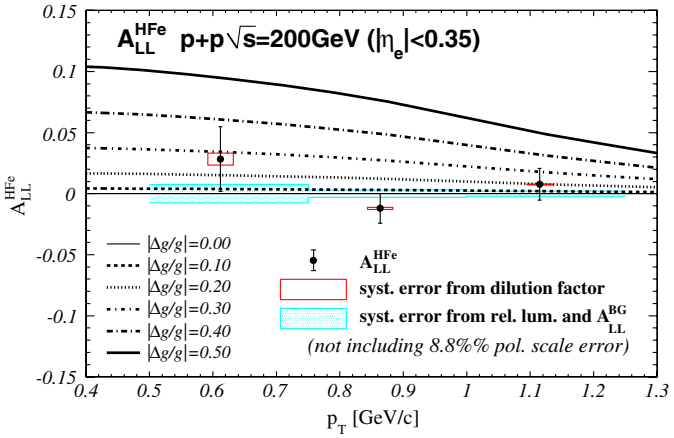

(a)Expected A_{LL}^{HFe} for several $|\Delta g/g|$.

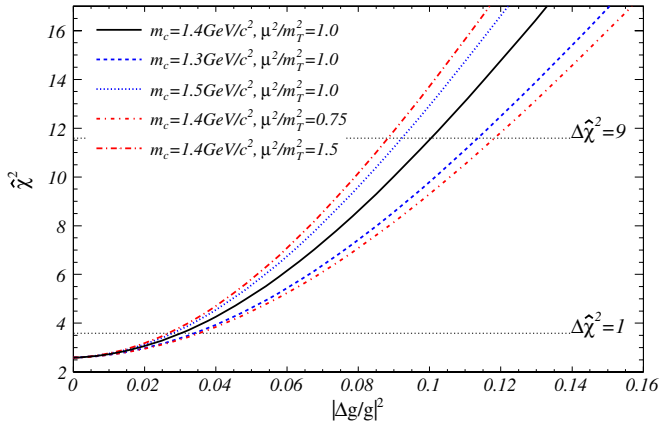

(b)$\hat{\chi}^2$ curves.

FIG. 15 (color online). (a) A_{LL}^{HFe} for $|\Delta g/g| = 0.00$, 0.10, 0.20, 0.30, 0.40, 0.50 are shown as the solid line, the dashed line, the dotted line, the dashed-dotted line, the long-dashed-dotted line and the dashed-triplicate-dotted line, respectively. They are plotted with the measured data points, and the notation for the error bars are same as Fig. 13. (b) $\hat{\chi}^2$ curves calculated from (a) as a function of $|\Delta g/g|^2$. The black solid line is the default configuration. The blue curves are after changing the charm mass to 1.3 GeV$/c^2$ (dashed line) and to 1.5 GeV$/c^2$ (doted line), and the red curves are after changing the scale μ^2 to $0.75m_T^{c2}$ (dashed-dotted line) and $1.5m_T^{c2}$ (long-dashed-dotted line).

more precisely in the future with higher statistics and higher beam polarizations.

VII. SUMMARY

We have presented a new analysis method for identifying heavy flavor electrons at PHENIX. With this new method, the signal purity is improved by a factor of about 1.5 around $0.75 \lesssim p_T \lesssim 2.00$ GeV$/c$ due to the rejection of photonic electrons by the HBD. We have reported on the first measurement of the longitudinal double-spin asymmetry of heavy flavor electrons, which are consistent with zero. Using this result, we estimate a constraint of $|\Delta g/g(\log_{10}x = -1.6^{+0.5}_{-0.4}, \mu = m_T^c)|^2 < 3.0 \times 10^{-2}(1\sigma)$. This value is consistent with the existing theoretical expectations with GRSV and DSSV. With improved statistics and polarization, the helicity asymmetry of heavy flavor electron production can provide more significant constraints on the gluon polarization and complement other measurements of ΔG.

ACKNOWLEDGMENTS

We thank the staff of the Collider-Accelerator and Physics Departments at Brookhaven National Laboratory and the staff of the other PHENIX participating institutions for their vital contributions. We thank Marco Stratmann for detailed discussions about constraining the gluon polarization and for the preparation of codes used to calculate the cross sections. We acknowledge support from the Office of Nuclear Physics in the Office of Science of the Department of Energy; the National Science Foundation; Abilene Christian University Research Council; Research Foundation of SUNY; Dean of the College of Arts and Sciences, Vanderbilt University (U.S.A); Ministry of Education, Culture, Sports, Science, and Technology and the Japan Society for the Promotion of Science (Japan); Conselho Nacional de Desenvolvimento Científico e Tecnológico and Fundação de Amparo à Pesquisa do Estado de São Paulo (Brazil); Natural Science Foundation of China (People's Republic of China); Ministry of Education, Youth and Sports (Czech Republic); Centre National de la Recherche Scientifique, Commissariat à l'Énergie Atomique and Institut National de Physique Nucléaire et de Physique des Particules (France); Bundesministerium für Bildung und Forschung, Deutscher Akademischer Austausch Dienst and Alexander von Humboldt Stiftung (Germany); Hungarian National Science Fund, OTKA (Hungary); Department of Atomic Energy and Department of Science and Technology (India); Israel Science Foundation (Israel); National Research Foundation and WCU program of the Ministry Education Science and Technology (Korea); Ministry of Education and Science, Russian Academy of Sciences, Federal Agency of Atomic Energy (Russia); VR and Wallenberg Foundation (Sweden); the U.S. Civilian Research and Development Foundation for the Independent States of the Former Soviet Union; the Hungarian American Enterprise Scholarship Fund and the US-Israel Binational Science Foundation.

[1] J. Ashman *et al.* (European Muon Collaboration), Phys. Lett. B **206**, 364 (1988).
[2] J. Ashman *et al.* (European Muon Collaboration), Nucl. Phys. B **328**, 1 (1989).
[3] J. Ellis and R. L. Jaffe, Phys. Rev. D **9**, 1444 (1974).
[4] J. Kodaira, Nucl. Phys. B **165**, 129 (1980).
[5] S. D. Bass, *The Spin Structure of the Proton* (World Scientific, Singapore, 1989).
[6] A. Airapetian *et al.* (HERMES Collaboration), Phys. Rev. D **75**, 012007 (2007).
[7] V. Y. Alexakhin *et al.* (COMPASS Collaboration), Phys. Lett. B **647**, 330 (2007).
[8] V. Y. Alexakhin *et al.* (COMPASS Collaboration), Phys. Lett. B **647**, 8 (2007).
[9] A. Adare *et al.* (PHENIX Collaboration), Phys. Rev. Lett. **103**, 012003 (2009).
[10] A. Adare *et al.* (PHENIX Collaboration), Phys. Rev. D **76**, 051106 (2007).
[11] S. S. Adler *et al.* (PHENIX Collaboration), Phys. Rev. D **73**, 091102 (2006).
[12] A. Adare *et al.* (PHENIX Collaboration), Phys. Rev. D **79**, 012003 (2009).
[13] A. Adare *et al.* (PHENIX Collaboration), Phys. Rev. D **83**, 032001 (2011).
[14] P. Djawotho *et al.* (STAR Collaboration), arXiv:1106.5769.
[15] B. I. Abelev *et al.* (STAR Collaboration), Phys. Rev. Lett. **100**, 232003 (2008).
[16] A. Adare *et al.* (PHENIX Collaboration), Phys. Rev. D **84**, 012006 (2011).
[17] A. Airapetian *et al.* (HERMES Collaboration), Phys. Rev. D **71**, 012003 (2005).
[18] M. Alekseev *et al.* (COMPASS Collaboration), Phys. Lett. B **660**, 458 (2008).
[19] D. de Florian, R. Sassot, M. Stratmann, and W. Vogelsang, Phys. Rev. D **80**, 034030 (2009).
[20] M. Karliner and R. W. Robinett, Phys. Lett. B **324**, 209 (1994).
[21] I. Bojak and M. Stratmann, Phys. Rev. D **67**, 034010 (2003).
[22] I. Bojak, arXiv:0005120.
[23] J. Riedl, A. Schafer, and M. Stratmann, Phys. Rev. D **80**, 114020 (2009).
[24] S. S. Adler *et al.* (PHENIX Collaboration), Phys. Rev. Lett. **96**, 032001 (2006).
[25] A. Adare *et al.* (PHENIX Collaboration), Phys. Rev. C **84**, 044905 (2011).
[26] K. Adcox *et al.*, Nucl. Instrum. Methods Phys. Res., Sect. A **499**, 469 (2003).
[27] K. Adcox *et al.*, Nucl. Instrum. Methods Phys. Res., Sect. A **499**, 480 (2003).
[28] K. Adcox *et al.*, Nucl. Instrum. Methods Phys. Res., Sect. A **499**, 489 (2003).
[29] M. Aizawa *et al.*, Nucl. Instrum. Methods Phys. Res., Sect. A **499**, 508 (2003).
[30] L. Aphecetche *et al.*, Nucl. Instrum. Methods Phys. Res., Sect. A **499**, 521 (2003).
[31] H. Akikawa *et al.*, Nucl. Instrum. Methods Phys. Res., Sect. A **499**, 537 (2003).
[32] M. Allen *et al.*, Nucl. Instrum. Methods Phys. Res., Sect. A **499**, 549 (2003).
[33] A. Kazlov, I. Ravinovich, L. Shekhtman, Z. Fraenkel, M. Inuzuka, and I. Tserruya, Nucl. Instrum. Methods Phys. Res., Sect. A **523**, 345 (2004).
[34] W. Anderson *et al.*, Nucl. Instrum. Methods Phys. Res., Sect. A **646**, 35 (2011).
[35] GEANT 3. 2. 1 Manual, http://wwwasdoc.web.cern.ch/wwwasdoc/pdfdir/geant.pdf (1994).
[36] A. Adare *et al.* (PHENIX Collaboration), Phys. Rev. D **83**, 052004 (2011).
[37] S. S. Adler *et al.* (PHENIX Collaboration), Phys. Rev. Lett. **91**, 241803 (2003).
[38] G. D. Lafferty and T. R. Wyatt, Nucl. Instrum. Methods Phys. Res., Sect. A **355**, 541 (1995).
[39] M. Cacciari, P. Nason, and R. Vogt, Phys. Rev. Lett. **95**, 122001 (2005).
[40] O. Jinnouchi *et al.*, arXiv:0412053.
[41] H. Okada *et al.*, Phys. Lett. B **638**, 450 (2006).
[42] H. Okada *et al.*, arXiv:0712.1389.
[43] A. Mukherjee, M. Stratmann, and W. Vogelsang, Phys. Rev. D **72**, 034011 (2005).
[44] T. Sjostrand *et al.*, arXiv:0710.3820.
[45] T. Sjostrand, S. Mrenna, and P. Skands, J. High Energy Phys. 05 (2006) 026.
[46] M. Glück, E. Reya, M. Stratmann, and W. Vogelsang, Phys. Rev. D **63**, 094005 (2001).
[47] J. Pumplin, D. R. Stump, J. Huston, H.-L. Lai, P. Nadolsky, and W.-K. Tung, J. High Energy Phys. 07 (2002) 012.